RESEARCH ARTICLE

Key Points:
- Energy spectra of coastal surface currents have decay slopes between k^{-2} and k^{-3} at a wave number (k) of 0.5 km^{-1}
- Injection scales estimated from submesoscale coastal surface current observations appear between 7 and 13 km
- High-frequency radar-derived surface currents as a practical and unique resource for submesoscale process studies

Correspondence to:
S. Y. Kim,
syongkim@kaist.ac.kr

Diagnostic Characteristics of Submesoscale Coastal Surface Currents

Hyun Sup Soh[1] and Sung Yong Kim[1] (iD)

[1]Environmental Fluid Mechanics Laboratory, Department of Mechanical Engineering, Korea Advanced Institute of Science and Technology, Yuseong-gu, Daejeon, Republic of Korea

Abstract Submesoscale kinetic energy (KE) spectra and fluxes at the length scales ranging from 2 to 25 km are estimated from hourly and O(1) km-scale coastal surface current maps observed from shore-based high-frequency radars off southern San Diego. The one-dimensional wave number-domain KE spectra of the surface currents have decay slopes between k^{-2} and k^{-3} at a wave number (k) of 0.5 km^{-1}. The KE spectra exhibit anisotropy associated with anisotropic circulation, which is constrained by the shoreline and bottom bathymetry. Moreover, the KE spectra exhibit weak seasonality related to the regional submesoscale eddies and low-frequency circulation with weak seasonal variability. The estimated KE fluxes are categorized into four cases of purely forward cascades and inverse cascades at all wave numbers, inverse-then-forward cascades with a single zero-crossing within the range of wave numbers (0.04 to 0.5 km^{-1}), and residuals, which account for approximately 33%, 39%, 19%, and 9% of the total number of realizations, respectively. An injection scale where forward enstrophy cascade and inverse energy cascade occur is estimated to be 5 to 10 km from the cases of the inverse-then-forward cascade, which is consistent with the length scales of the regional submesoscale eddies. Thus, the regional submesoscale processes are initiated by surface frontogenesis due to the weak seasonal low-frequency surface circulation and topography-related currents, then maintained by baroclinic instabilities associated with the seasonal mixed layer and O(10) km-scale submesoscale eddies with weak seasonal variability.

1. Introduction

Mesoscale oceanic variability involves ocean dynamics that occur at scales relevant to the rotation of the Earth, i.e., scales within a small Rossby number regime (R_o; $R_o = \zeta/f_c$, where ζ and f_c represent the vertical components of relative and planetary vorticity, respectively; e.g., Pedlosky, 1992; Woods, 1980). Studies on mesoscale oceanic processes have been increased with the advent of high-precision satellite altimeters and radiometers (e.g., Chelton & Schlax, 1996; Munk et al., 2000) and theoretical frameworks (e.g., Held et al., 1995; Vallis, 2006). Conversely, submesoscale oceanic features, which are frequently observed as filaments, fronts, and eddies, are characterized by both the O(1) Rossby number and a horizontal scale smaller than the first baroclinic Rossby deformation radius (e.g., Levy et al., 2012; Thomas et al., 2009). Submesoscale processes are important because they contribute to the vertical transports of oceanic tracers, mass, and buoyancy and rectify both the mixed layer structure and upper ocean stratification (e.g., Hoskins & Bretherton, 1972; McWilliams, 1985). The generation mechanisms of submesoscale processes have been described with mesoscale eddy-derived surface frontogenesis, baroclinic instabilities in the mixed layer, topographically linked vortices, and turbulent thermal winds (e.g., Callies et al., 2015; McWilliams, 2016; Thomas et al., 2009). The studies on these submesoscale processes have benefited primarily from idealized numerical models under relevant theoretical frameworks (e.g., Mahadevan & Tandon, 2006; Tulloch & Smith, 2006) because they require high-resolution data of less than one hour in time and O(1) km in space. The in situ observations at these scales are limitedly available in both number and size when compared with the numerical model outputs (e.g., Buckingham et al., 2016; D'Asaro et al., 2011; Haza et al., 2010; Kim, 2010; Lekien & Coulliette, 2007; Shcherbina et al., 2013).

Since the availability of submesoscale observations is limited and the present-day satellite altimetry (ALT) observations primarily cover mesoscale processes, the kinetic energy (KE) spectra at the submesoscale are not fully understood (e.g., Callies et al., 2015; Le Traon et al., 2008; Stammer, 1997; Xu & Fu, 2012; Zhou

et al., 2015). Stammer (1997) examined the globally averaged wave number-domain KE spectra of the ALT-derived cross-track geostrophic currents and reported that their decay slopes vary between k^{-1} (100 < L < 300 km, where k and L denote the wave number and length scale, respectively) and either k^1 (observational noise) or k^{-2} (optimal filter) at scales of less than 100 km (L < 100 km). Le Traon et al. (2008) showed that the KE spectra of the ALT-derived cross-track geostrophic currents in regions of high eddy activity have a decay slope of $k^{-5/3}$ (100 < L < 300 km). Based on the spectral decay slopes, these authors hypothesized that ALT observations are better explained by surface quasi-geostrophic (sQG) dynamics than by quasi-geostrophic (QG) theory. Wang et al. (2010) reported that the KE spectra estimated from the ship-board acoustic Doppler current profiler (ADCP) currents and ALT-derived cross-track geostrophic currents in the Gulf Stream region exhibit k^{-3} and k^{-2} slopes, respectively. These authors interpreted that this difference may result from noise in the ALT observations and the two-dimensional QG theory was a superior dynamical framework to the sQG theory for explaining in situ observations. Kim et al. (2011) showed that the KE spectra of the coastal surface currents have a continuous transition from mesoscale to submesoscale that ranged from scales of 2 to 2,000 km and a decay slope of k^{-2}, which were obtained from a network of high-frequency radars (HFRs) off the west coast of the U.S. (within 150 km of the coast). Similarly, Callies and Ferrari (2013) reported that (1) the KE spectra of the currents in the Gulf Stream and subtropical North Pacific region have decay slopes of k^{-3} and k^{-2}, respectively, and (2) the ocean currents are described with geostrophic turbulent flows at large scales (50–200 km) and internal waves at small scales (less than 1 km), based on the wave-vortex and Helmholtz decompositions (e.g., Buhler et al., 2014; Lindborg, 2015) on the transects of the shipboard ADCP currents (see Appendix A for the theoretical spectral decay slopes of the geophysical turbulent flows).

Regarding the pathways of energy and enstrophy (the integral of the square of the vorticity) in geostrophic turbulent flows (Figure 1a), the energy cascades toward smaller scales in a baroclinic mode (e.g., the first baroclinic deformation of the radius for baroclinic instability) and is partially transformed into barotropic energy. Then, the barotropic energy cascades toward larger scales. The remaining forward cascading energy reaches the dissipation scales along with the conversion of available potential energy (APE) into eddy kinetic energy (EKE), and a portion of the EKE is partially converted into barotropic energy via the inverse cascade. In contrast, the enstrophy cascades toward small scales into the baroclinic and barotropic modes. During the transition of the energy and enstrophy through spatial scales, an injection scale (or a separation length scale) is defined as the length scale at which forward enstrophy cascade and inverse energy cascade occur (e.g., Ferrari & Wunsch, 2009; Larichev & Held, 1995; Rhines, 1977; Salmon, 1998; Scott & Wang, 2005; Vallis, 2006; Venaille et al., 2011). For instance, most of the energy in the ocean remains in the baroclinic
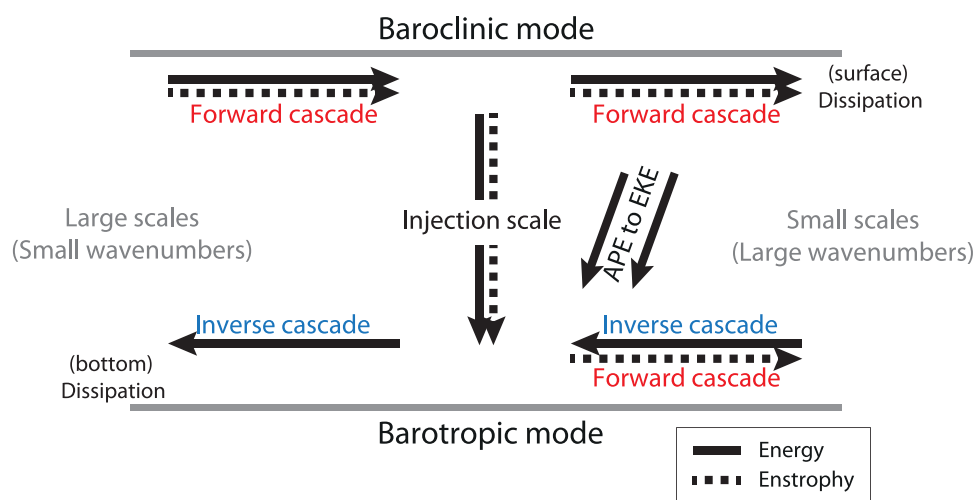

Figure 1. Pathways of energy and enstrophy in geostrophic turbulence. An injection scale is defined as the length scale where forward enstrophy cascade and inverse energy cascade occur. Solid and dash lines indicate energy and enstrophy, respectively, and the arrow denotes the direction of cascades. Available potential energy (APE) is converted into eddy kinetic energy (EKE) (e.g., Ferrari & Wunsch, 2009; Rhines, 1977; Salmon, 1998; Scott & Wang, 2005; Vallis, 2006; Wunsch, 2015).

mode, and the nonlinear evolution of baroclinic instabilities leads to an inverse cascade of energy (e.g., Gill et al., 1974; Smith & Vallis, 2002). Scott and Wang (2005) reported that an inverse cascade appears near the Rossby deformation radius (e.g., 100 to 150 km in the midlatitude region) based on the KE flux estimates of the gridded ALT-derived geostrophic currents, even though the gridded geostrophic currents include unrealistic variability at scales smaller than 100 to 300 km (e.g., Arbic et al., 2012; Stammer, 1997; Wortham & Wunsch, 2014). In describing the two primary mechanisms of the submesoscale processes, the frontogenesis associated with mesoscale eddies and baroclinic instability associated with the mixed layer have spatial scales of $O(100)$ and $O(10)$ km, respectively (e.g., Callies et al., 2015; McWilliams, 2016; Vallis, 2006), which can be candidate length scales to uniquely characterize the submesoscale processes. Klein et al. (2008) reported that the injection scales appear to be approximately 30 km based on numerical simulations under the sQG theory. However, the mesoscale-to-submesoscale energy pathways and the relevant injection scales have not yet been fully quantified with in situ submesoscale observations (e.g., Wunsch & Ferrari, 2004).

We investigate (1) the submesoscale wave number-domain KE spectra and fluxes as diagnostic characteristics of the submesoscale coastal surface currents and (2) the oceanic injection scales below 100 km based on the estimated KE fluxes. Thus, we mainly analyze the coastal surface currents with a spatial resolution of $O(1)$ km and a temporal resolution of one hour obtained from shore-based HFRs. The paper is divided into five sections. The HFR-derived coastal surface currents and the applied decomposition techniques are described in section 2, and the wave number-domain KE spectra and fluxes are presented with their methodological descriptions, estimates, and interpretations in sections 3 and 4, respectively. Finally, a discussion of the results and a summary follow in sections 5 and 6, respectively.

2. Data

2.1. Surface Currents

Hourly averaged radial velocity maps with a spatial resolution of 1.5 km and an azimuthal resolution of 5° were obtained from three local HFRs along the coast of southern San Diego. These radial velocity maps were optimally interpolated into a surface vector current map with a spatial resolution of 1 km using an exponential correlation function with an isotropic decorrelation length scale of 2 km to minimize spatial smoothing (Kim et al., 2007, 2008; Figure 2a). The uncertainty of the HFR-derived surface currents in the study area is less than 6 cm s^{-1}, which was estimated from the standard deviations of the sum of the oppositely facing radial velocity pairs sampled at nearby radial grid points by two independent radars (e.g., Kim, 2015; Kim et al., 2008; Paduan et al., 2006). An hourly averaged radial velocity was obtained from a temporal mean of at most six samples of the radial velocities within 1 h because of the irregular occurrence of missing data in both time and space (e.g., Kim et al., 2008; Schmidt, 1986).

Since the HFR-derived surface currents contain responses to primary geophysical forces (e.g., tides and wind stress) and their interactions (e.g., Kim et al., 2010a, 2011), we decompose the observed surface currents in terms of their driving forces and interpret their KE spectra and fluxes. The total surface currents ($\mathbf{u}$) are statistically decomposed into components coherent with pure tides ($\mathbf{u}_T$) and local wind stress ($\mathbf{u}_W$), in the low ($\mathbf{u}_{\hat{L}}$), diurnal ($\mathbf{u}_{\hat{D}}$), and semidiurnal ($\mathbf{u}_{\hat{S}}$) frequency bands, and residuals ($\mathbf{u}_R$) (see Kim et al., 2010a for further details),

$$\mathbf{u}(t) = \mathbf{u}_T(t) + \mathbf{u}_W(t) + \mathbf{u}_{\hat{L}}(t) + \mathbf{u}_{\hat{D}}(t) + \mathbf{u}_{\hat{S}}(t) + \mathbf{u}_R(t), \qquad (1)$$

using frequency-domain analyses, including the wind transfer function analysis (e.g., local wind-coherent components), harmonic analysis (e.g., barotropic tides), and slow finite Fourier transform (FFT) on the three frequency bands (e.g., low [$|\sigma| \leq 0.4$ cycles per day (cpd)], diurnal [$0.8 \leq |\sigma| \leq 1.2$ cpd], and semidiurnal [$1.7 \leq |\sigma| \leq 2.2$ cpd] frequency bands, where σ denotes the frequency axis; e.g., Kim, 2010; Kim et al., 2010a) instead of using simple band-pass filtering in the wave number domain or frequency domain. Examples of the decomposed surface current time series for a period of 10 days (yeardays of 146 to 155 in 2003) are shown in Figure 3.

The frequency-wave number-domain KE spectrum [$S(\sigma, k)$] and frequency-domain KE spectrum [$S(\sigma)$] of the total surface currents for a period of two years (April 2003 to March 2005) within a white box in Figure 2a indicate that the primary variances are clustered in these three frequency bands and spread through all
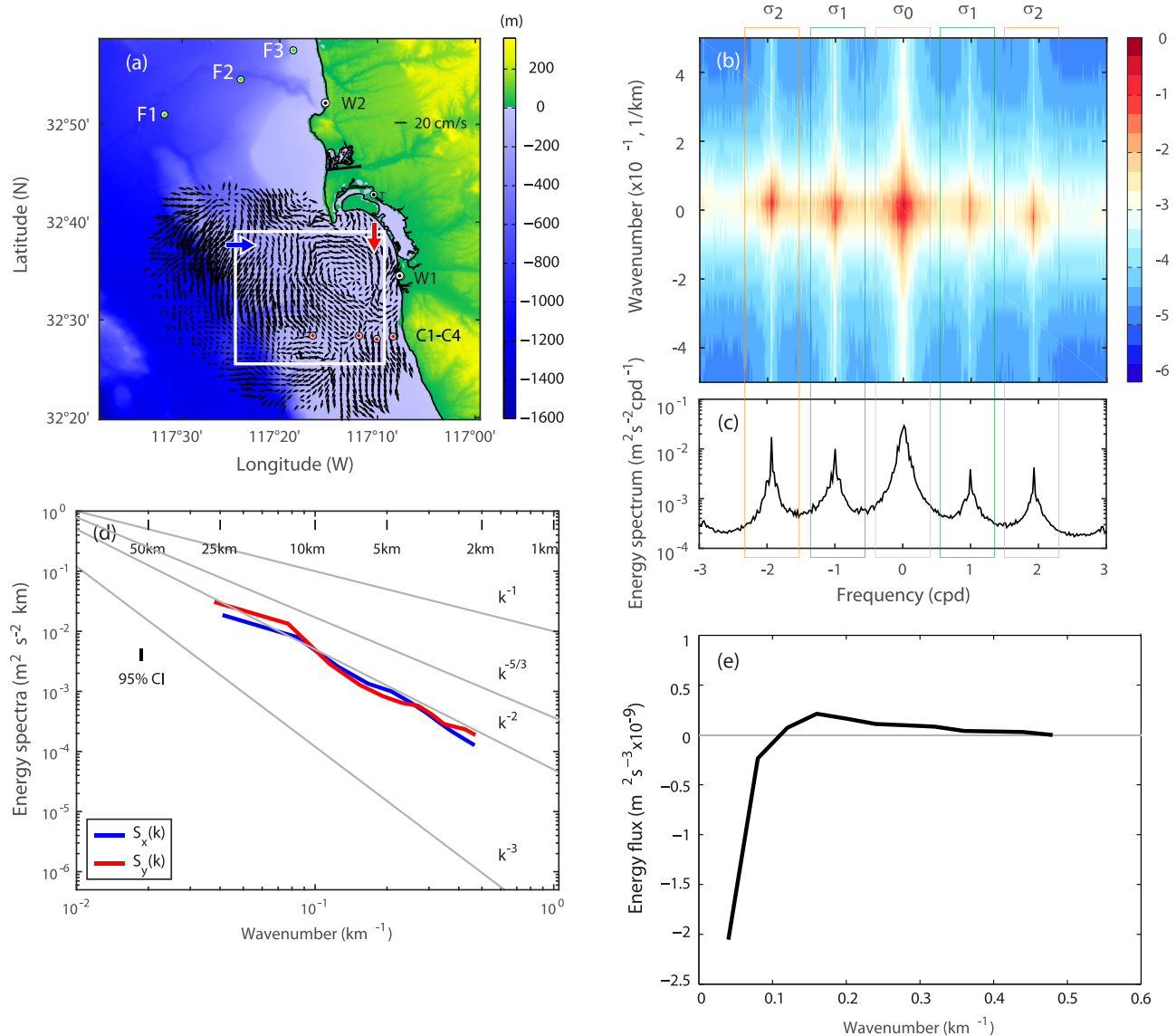
Figure 2. Examples of an observed HFR-derived surface current map, frequency-wave number-domain KE spectrum, frequency-domain KE spectrum, wave number-domain KE spectra, and KE fluxes of the total surface currents. (a) A map of HFR-derived surface currents sampled at 1600 (GMT) on 1 February 2004. CTD sampling stations and shore-based wind stations are marked: C1, C2, C3, and C4 for SBOO (red dots) and F1, F2, and F3 for CalCOFI Line 93.3 (green dots); W1 for Tijuana River Valley and W2 for Scripps Pier (black dots). (b) Frequency-wave number-domain KE spectrum ($S(\sigma, k)$, $\log_{10}$ scale, $m^2 s^{-2} cpd^{-1}$ km). (c) Frequency-domain KE spectrum ($S(\sigma)$, $m^2 s^{-2} cpd^{-1}$). Three primary frequency bands (low [σ_0: $|\sigma| \leq 0.4$ cpd], diurnal [σ_1: $0.8 \leq |\sigma| \leq 1.2$ cpd], and semidiurnal [σ_2: $1.7 \leq |\sigma| \leq 2.2$ cpd] frequency bands, where σ denotes the frequency axis) are marked with colored boxes in Figures 2b and 2c. (d) Wave number-domain KE spectra ($S_x(k)$ and $S_y(k)$, $m^2 s^{-2}$ km). Surface currents are sampled on multiple one-dimensional cross-shore lines (a direction following a blue arrow in Figure 2a) and are averaged in the alongshore direction to estimate the wave number-domain KE spectrum ($S_x(k)$) in the cross-shore direction. Similarly, $S_y(k)$ is the cross-shore-directional average of the KE spectra estimated from surface currents sampled in the alongshore direction (a direction following a red arrow in Figure 2a). Length scales of 1, 2, 5, 10, 25, and 50 km are marked on the top, and gray auxiliary lines denote the spectral decay slopes of k^{-1}, $k^{-5/3}$, k^{-2}, and k^{-3}. A 95% confidence interval (CI) of individual KE spectra is indicated. (e) KE fluxes ($\Pi(k)$). Note that the frequency-wave number-domain and frequency-domain KE spectra in Figures 2b and 2c are computed from the hourly surface currents within a white box in Figure 2a for a period of two years (April 2003 to March 2005; 17,544 realizations), and the KE spectra and fluxes in Figures 2d and 2e are estimated from a single realization of the surface currents within the same white box in Figure 2a.

wave numbers (Figures 2b and 2c). In general, nonlinear interactions of oceanic processes are described in the broadband frequency and wave number domains (e.g., Longuet-Higgins et al., 1967); however, these interactions can be considered in specific frequency bands or primary wave numbers if their variances of interest are already known, as shown in Figure 2b. In particular, the energy in geostrophic turbulence can be transferred to neighboring wave numbers via nonlinear interactions based on classical turbulence theories (e.g., Wunsch, 2015). As the decomposition of the surface currents is conducted in the frequency
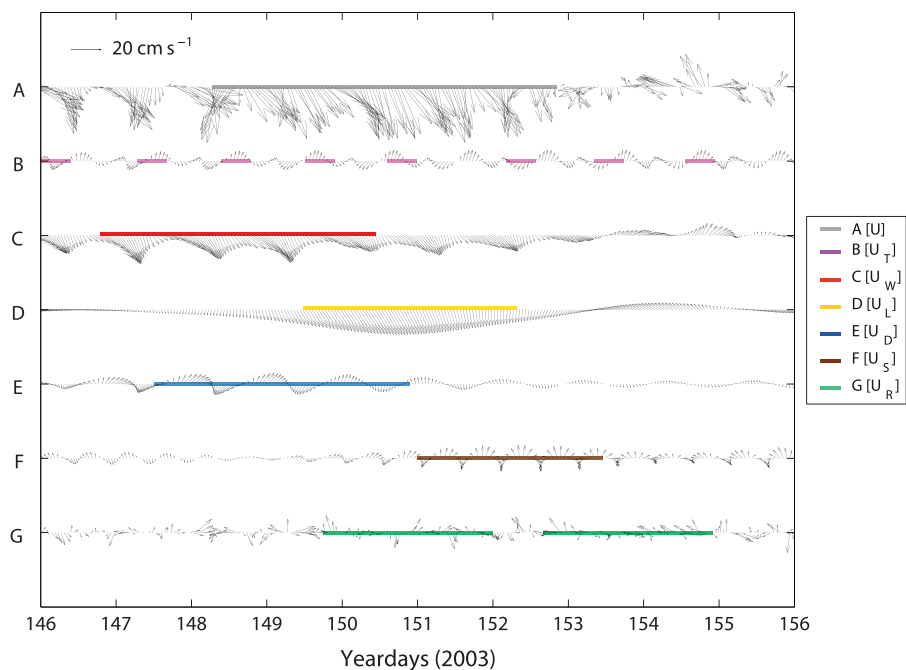
Figure 3. Examples of statistically decomposed surface currents for a period of 10 days (yeardays of 146 to 155 in 2003; excerpt from Kim et al., 2010a, Figure 4). The time windows with a single zero-crossing in the estimated KE fluxes of the decomposed surface currents are marked with colors. Individual components of the decomposed surface currents are indicated: total surface currents ($\mathbf{u}$; A), surface currents coherent with pure tides ($\mathbf{u}_T$; B) and local wind stress ($\mathbf{u}_W$; C), surface currents in the low ($\mathbf{u}_L$; D), diurnal ($\mathbf{u}_D$; E), and semidiurnal ($\mathbf{u}_S$; F) frequency bands, and residual surface currents ($\mathbf{u}_R$; G).

domain in this paper, the individual surface current components contain variance at all spatial scales, i.e., the decomposed surface current components are not limited to a specific spatial scale. Thus, in our analysis, nonlinear interactions associated with energy exchange at all wave numbers are allowed within each decomposed component or specific frequency bands because the decomposed surface currents fully represent the direct responses of the ocean to the driving forces. For instance, the scale-by-scale interactions of the near-inertial surface currents within the chosen frequency band and all wave numbers have been examined elsewhere (e.g., Kim & Kosro, 2013) and can also be examined in our analysis. In other words, in our analysis, the scale-by-scale interactions between tide-driven and wind-driven surface currents cannot be examined because (1) the applied decomposition analysis separates the variance using a coherent relationship between the direct driving force and the response and (2) we do not implement a method to separate the overlapping and interrelated variance associated with individual driving forces. The slow FFT indicates a least squares fit that uses orthogonal basis functions for all available frequencies and ensures that the unevenly sampled data and the data with missing observations are treated appropriately. Although the surface current data in the study domain have been available since 2003, the quality assurance and quality controlled (QAQC'd) and statistically decomposed surface current data set for only two years is available for scientific analyses (e.g., Kim et al., 2010a, 2010b). The wind transfer functions are the regression coefficients in the frequency domain between surface currents and wind stress at the Scripps Pier (W1) and Tijuana River (W2), as shown in Figure 2a (see Kim et al., 2010a, 2010b, 2015 for more details). The Hanning window function is applied to estimate the KE spectra (section 3.1) and KE fluxes (section 4.1) to prevent low-frequency variance from contaminating the estimates of the KE spectra. Although the use of the window function can reduce the original variance, it will produce unambiguous estimates in the spectral decay slope of the wave number-domain KE spectra (e.g., Harris, 1978; Priestley, 1981; see section 5.4 for more details).

2.2. Conductivity-Temperature-Depth (CTD) Data
Seasonal stratification and seasonal time windows are determined from a regression analysis of temperature and salinity profiles obtained from hydrographic surveys of the California Cooperative Oceanic Fisheries Investigation (CalCOFI) and the South Bay Ocean Outfall (SBOO) in the study domain (Kim & Cornuelle, 2015).
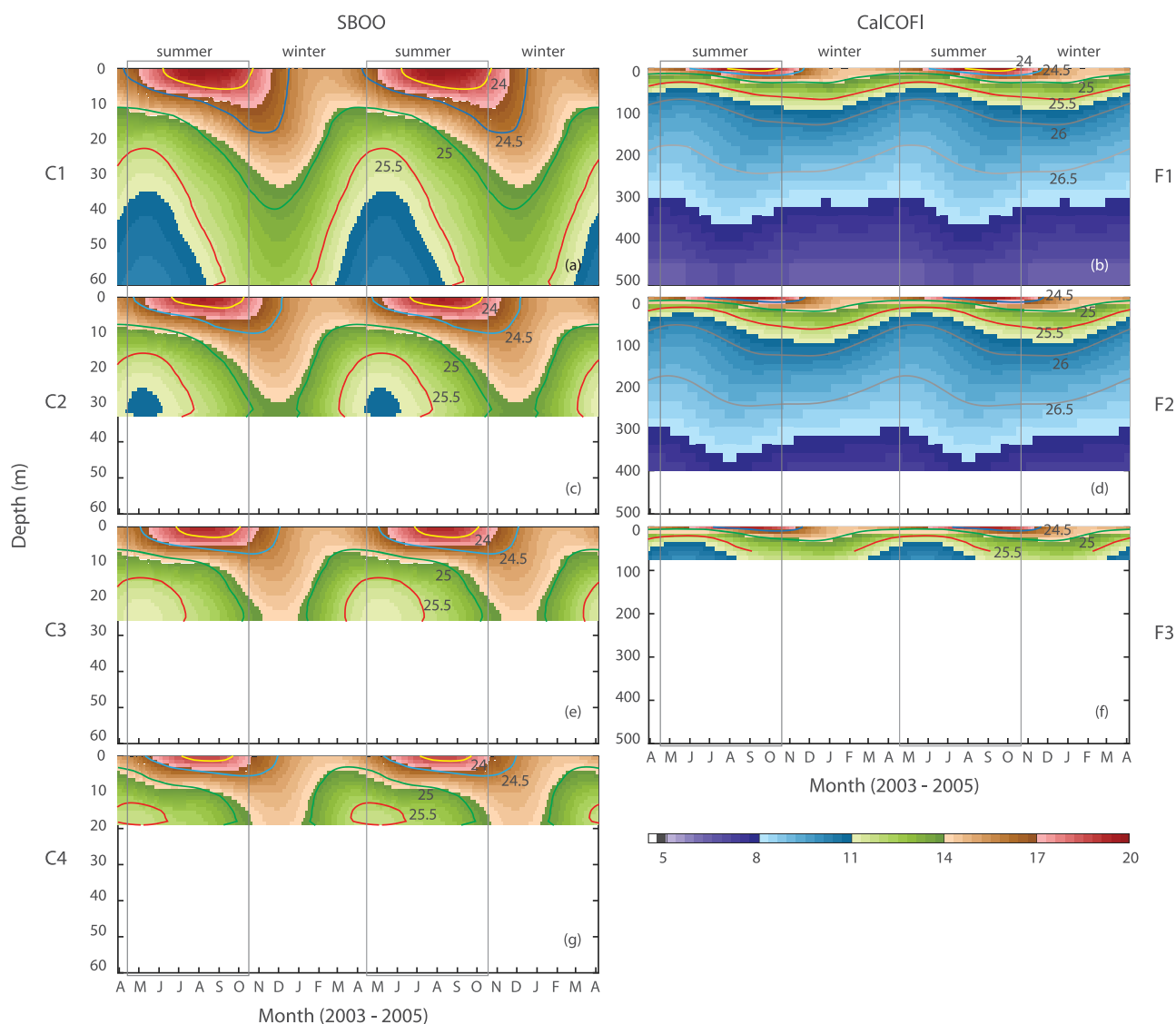
Figure 4. Time series of reconstructed temperature profiles (°C) on a three-daily time axis at (a) C1, (c) C2, (e) C3, and (g) C4 stations for SBOO and (b) F1, (d) F2, and (f) F3 stations for CalCOFI (Figure 2a). Constant density anomalies of 24 (yellow), 24.5 (blue), 25.0 (green), 25.5 (red), and higher than 26.0 (gray) kg m^{-3} are overlaid with colors with an interval of 0.5 kg m^{-3}. Seasonal time windows for the summer (15 April to 14 October) and winter (15 October to 14 April) are marked. Note that seasonally averaged profiles of temperature, salinity, density, and buoyancy frequency at C1 have been reported elsewhere (Kim et al., 2010b, Figure 4).

The monthly (SBOO) and quarterly (CalCOFI) sampled time series for the most recent 7 to 50 years (2003 to 2009 for SBOO and 1950 to 2009 for CalCOFI) are regressed with the time series of trigonometric functions at the seasonal frequency and five seasonal superharmonic frequencies, primary climate indices (e.g., El Niño-Southern Oscillation [ENSO], Pacific Decadal Oscillation [PDO], North Pacific Gyre Oscillation [NPGO], and Scripps Pier temperature), and a linear trend. The time series of the temperature profiles for a period of two years (April 2003 to March 2005) are reconstructed using identical basis functions (see Kim & Cornuelle, 2015 for more details; Figure 4). The seasonal variability of vertical stratification and the mixed layer depths is nearly uniform in the cross-shore direction and consistent across the independent CTD samplings (SBOO and CalCOFI). The seasonal time windows are determined with a six month time window centered around the maximum and minimum temperatures of the year on 15 July and 15 January for the summer and winter, respectively. In the study domain, the seasonal thermocline remains near 5 and 25 m, and the maximum of the buoyancy frequency appears near 10 m for the summer and 25 m for the winter, as reported elsewhere (e.g., Kim et al., 2010b, Figure 4). Color-coded constant density anomalies of 24.0 to 26.5 kg m^{-3} with an interval of 0.5 kg m^{-3} are marked to represent the variability of the seasonal mixed layer (Figure 4).

3. KE Spectra

One-dimensional wave number-domain KE spectra of the coastal surface currents (length scales of 2 to 25 km in this paper) are examined in terms of (1) frequency bands (e.g., subinertial and superinertial frequency bands) and potential drivers (e.g., tides, winds, and low-frequency forces) associated with the scale of variability, (2) anisotropy (e.g., sampling directions of the surface currents [cross-shore and along-shore directions] and individual current components [u and v, where u and v denote the zonal and meridional current components, respectively, without any rotations]) related to the influence of coastal boundaries (e.g., bottom bathymetry and the shoreline), and (3) seasonality (e.g., summer and winter) associated with regional stratification and potential mechanisms that drive the regional submesoscale processes (e.g., mesoscale and submesoscale eddies and mixed layer instabilities). Thus, we evaluate the one-dimensional wave number-domain KE spectra of (1) the total surface currents in the subinertial and superinertial frequency bands, (2) the individual components (u and v) of the total surface currents, (3) the seasonal total surface currents, and (4) the statistically decomposed surface currents. We extend these analyses into a two-dimensional wave number-domain by examining the decorrelation length scales of the two-dimensional covariance, which is equivalent to the two-dimensional wave number-domain KE spectrum (see Appendix B).

3.1. Estimates of KE Spectra

The KE power spectral density functions (referred to as KE spectra below) of the surface currents ($\mathbf{u}=u+iv$) sampled on multiple cross-shore lines (the direction following the blue arrow in Figure 2a) are averaged in the alongshore direction to estimate the one-dimensional wave number-domain (k) KE spectrum ($\mathcal{S}_x(k, t_l)$) at a time (t_l) in the cross-shore direction:

$$\mathcal{S}_x(k, t_l) = \frac{1}{N} \sum_{n=1}^{N} \left[\frac{1}{\Delta k} \left| \frac{1}{M} \sum_{m=0}^{M-1} \mathbf{u}(x_m, y_n, t_l) e^{-ikx_m} \right|^2 \right], \tag{2}$$

where x and y denote the cross-shore and alongshore directions, respectively, and M and N indicate the number of sampling grid points in the corresponding directions.

Similarly, the cross-shore-directional average of the KE spectra ($\mathcal{S}_y(k, t_l)$) at one time, which are estimated from surface currents sampled on multiple alongshore lines (the direction following the red arrow in Figure 2a), is defined as

$$\mathcal{S}_y(k, t_l) = \frac{1}{M} \sum_{m=1}^{M} \left[\frac{1}{\Delta k} \left| \frac{1}{N} \sum_{n=0}^{N-1} \mathbf{u}(x_m, y_n, t_l) e^{-iky_n} \right|^2 \right]. \tag{3}$$

These KE spectra in the individual directions are averaged over realizations ($L \geq 1$):

$$S_x(k) = \frac{1}{L} \sum_{l=1}^{L} \mathcal{S}_x(k, t_l), \tag{4}$$

$$S_y(k) = \frac{1}{L} \sum_{l=1}^{L} \mathcal{S}_y(k, t_l). \tag{5}$$

Although the wave-vortex decomposition can isolate the unbalanced wave motions and balanced motions in the submesoscale current fields, it is not included in the evaluation of the diagnostic characteristics in this paper (e.g., Buhler et al., 2014; Callies & Ferrari, 2013) because it requires assumptions that the data are stationary, homogeneous, and horizontally isotropic, which may not be valid for the regional surface currents (e.g., Kim et al., 2007, 2009, 2010a).

3.2. Estimates of Spectral Decay Slopes

The temporal variability of the spectral decay slopes is presented in two wave number ranges ($0.04 \leq k_{1,x} \leq 0.085$ km^{-1} and $0.1 \leq k_2 \leq 0.33$ km^{-1} for $S_x(k)$; $0.03 \leq k_{1,y} \leq 0.097$ km^{-1} and $0.1 \leq k_2 \leq 0.33$ km^{-1} for $S_y(k)$). The spectral decay slopes are regressed with a constant, and the temporal mean and standard errors of the estimated spectral decay slopes within a 10 day time window are shown in Figures 5b and 5c for S_x and S_y, respectively. The expected spectral decay slopes of $k^{-5/3}$ (red) and k^{-3} (blue)
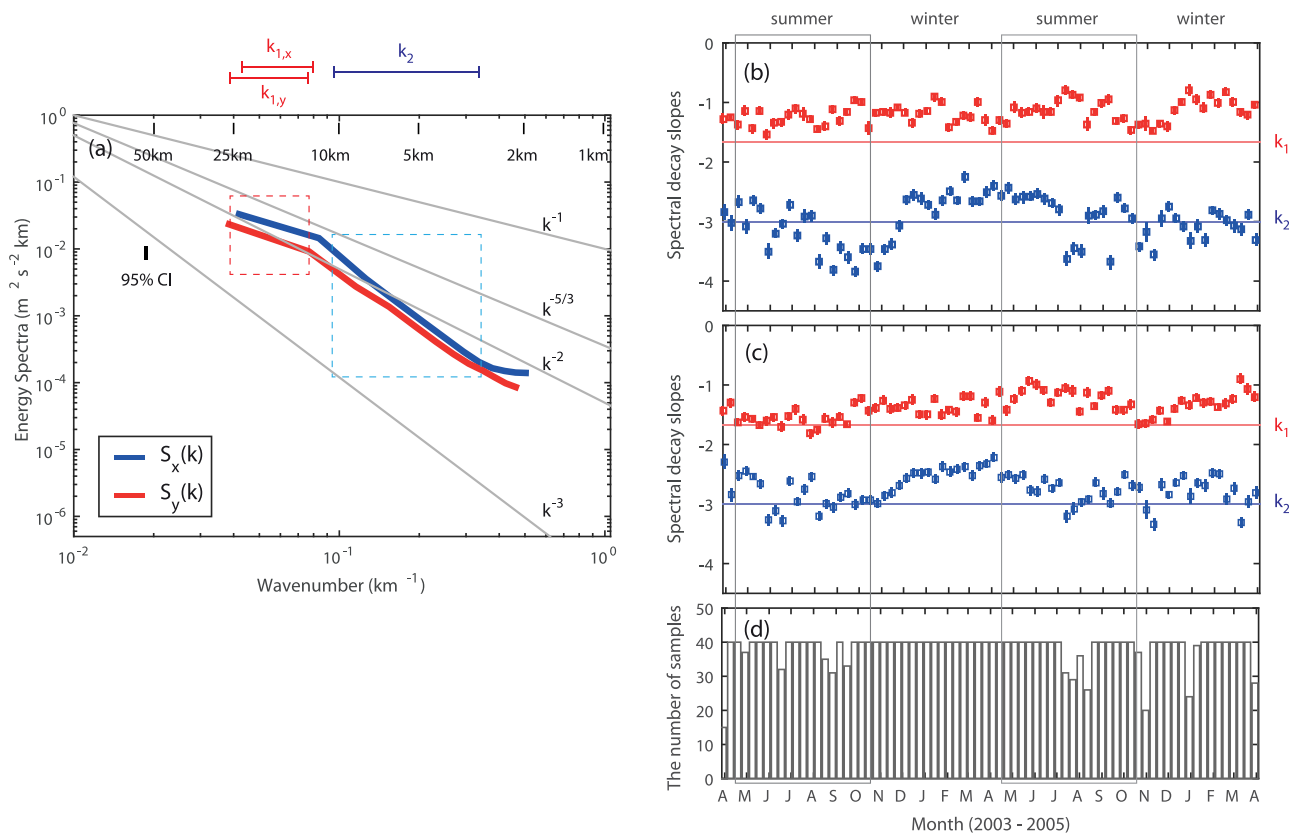
Figure 5. (a) Wave number-domain KE spectra of the surface currents are averaged over the entire year ($S_x(k)$ for cross-shore direction [blue] and $S_y(k)$ for alongshore direction [red]; see Figure 2a for sampling directions). Length scales of 1, 2, 5, 10, 25, and 50 km are marked on the top, and gray auxiliary lines denote the spectral decay slopes of k^{-1}, $k^{-5/3}$, k^{-2}, and k^{-3}. A 95% confidence interval (CI) of individual KE spectra is indicated. (b, c) Spectral decay slopes ($S_x(k)$ in Figure 5b and $S_y(k)$ in Figure 5c) are estimated from the KE spectra of the surface currents using a least squares fit in individual wave number ranges ($0.04 \leq k_{1,x} \leq 0.085$ km^{-1} [red] and $0.1 \leq k_2 \leq 0.33$ km^{-1} [blue] for $S_x(k)$; $0.03 \leq k_{1,y} \leq 0.097$ km^{-1} [red] and $0.1 \leq k_2 \leq 0.33$ km^{-1} [blue] for $S_y(k)$), and the temporal mean and standard errors of the estimated spectral decay slopes within a 10 day-long time window are presented with a colored square and vertical line, respectively. The expected spectral decay slopes ($k^{-5/3}$ [red] and k^{-3} [blue]) based on the QG theory are plotted with colored horizontal lines. (d) The number of surface current maps participating in the estimate of the spectral decay slopes within a 10 day time window. Seasonal time windows for the summer (15 April to 14 October) and winter (15 October to 14 April) are marked in Figures 5b to 5d. All estimates are based on the six-hourly averaged surface currents for a period of 2 years (April 2003 to March 2005; 2,924 realizations).

based on the QG theory are marked (see section 5.1 and Appendix A for more details on the distinction of the appropriate theoretical framework). For better estimates of the spectral decay slopes, six-hourly averaged surface current maps are used to estimate the KE spectra because the chosen time window can (1) maintain the regional diurnal and semidiurnal variability of the surface currents and (2) improve the signal-to-noise ratios (SNRs) within the chosen wave number ranges. The selected low-wave number ranges differ because the wave number axes are not identical due to the nonsquare dimensions of the sampling domain.

3.3. Interpretation of the Estimated KE Spectra

The KE spectra (S_x and S_y) in Figure 2d are estimated from a single realization of the surface currents within the white box in Figure 2a, which has a submesoscale eddy with a radius of approximately 10 km. The two orthogonally sampled and averaged KE spectra have consistent variance and decay slopes of k^{-2} with a minor difference in the sampling directions (Figure 2d). This is within the range of spectral decay slopes of the KE spectra of the submesoscale currents, which are k^{-2} in theories and numerical simulations (e.g., McWilliams, 1985) or k^{-3} in observations (e.g., Callies et al., 2015; Ishihara & Kaneda, 2001; Lekien & Coulliette, 2007; Tung & Orlando, 2003). Similarly, the KE spectra of the surface currents are averaged over a period of two years (Figure 5a) and their spectral decay slopes are between k^{-2} and k^{-3} at a wave number of 0.5 km^{-1}.

The time series of the estimated spectral decay slopes of the six-hourly averaged surface currents over the 2 years fluctuate between k^{-1} and k^{-2} in the k_1 wave number range and between k^{-2} and k^{-3} in the k_2 wave number range, and these decay slopes have weak seasonality that is modulated by higher harmonics of seasonal variability. Callies et al. (2015) reported that the spectral decay slopes of the KE spectra in the summer become steeper than those in the winter as the instabilities within the shallower mixed layer in the summer are easily damped out. In particular, the decay slope under summer stratification is close to k^{-3} in the length scale of 20–200 km (k_1 wave number range) and k^{-2} in the length scale below 20 km (k_2 wave number range), and these decay slopes are slightly different from the temporal variability in Figures 5b and 5c. The time series of the estimated spectral decay slopes provide a comprehensive view to explain the cases of a single realization of k^{-2} (Figure 2d) and two year realizations of between k^{-2} and k^{-3} (Figure 5a) and better statistical confidence in the estimates (Figures 5b and 5c). The number of vector current maps for the estimates of the spectral decay slopes does not show any seasonal bias (Figure 5d).

The surface current time series in the subinertial and superinertial frequency bands are obtained from a running mean using a nonoverlapping daily time window and their residuals, respectively, which may result in the smearing of submesoscale processes at time scales shorter than one day (The local Coriolis frequency is equal to 1.07 cpd). The KE spectra of the subinertial surface currents follow a k^{-3} decay slope (Figure 6a), which may represent the oceanic responses to the low-frequency and synoptic-scale forcings (e.g., large-scale winds and barotropic tides) and be explained with two-dimensional QG theory (e.g., Charney, 1971; Gage, 1979) or a steepened slope associated with interior currents under sQG theory (e.g., Callies et al., 2015). Conversely, the spectral decay slopes of the superinertial surface currents are $k^{-5/3}$ or k^{-2} (Figure 6b), which can comprise the responses to relatively high-frequency forcing (e.g., baroclinic tides, local winds, and noise) and be interpreted by the contribution of mixed layer instabilities (e.g., Boccaletti et al., 2007) or the nonlinear interactions of internal waves (e.g., Callies & Ferrari, 2013).

The KE spectra of the individual current components (u and v) have a decay slope between k^{-2} and k^{-3} with minor differences in the current components and sampling directions (Figure 6b), which can be explained by the anisotropy of the regional surface circulation that results from coastal boundary effects (e.g., bottom bathymetry and the shoreline; e.g., Kim et al., 2010a). The KE spectrum ($S_{x,v}(k)$) of the alongshore surface currents sampled in the cross-shore direction has more variance than other components, which can be explained by the regionally dominant alongshore currents that have a cross-shore gradient. In this region, the submesoscale eddies with diameters of 5 to 15 km and Rossby number magnitudes of 0.2 to 2 are primarily generated by the regional low-frequency currents and their topographically linked variability (Kim, 2010). For instance, the intrusion of regional low-frequency currents generates clockwise eddies that are caused by eastward currents at the northern boundary and counterclockwise eddies related to interactions between southward currents rolling over the headland (or at the trailing edge) and nearshore northward countercurrents. The anisotropic KE spectra motivate an investigation of the spectral decay slopes of the one-dimensional wave number-domain KE spectra in multiple directions using two-dimensional spatial correlations (see Appendix B).

The spectral decay slopes of the seasonal KE spectra do not show a seasonal difference varying between k^{-2} and k^{-3} within the confidence interval (Figure 6c). This result suggests that the regional submesoscale processes are (1) initiated by surface frontogenesis due to weak seasonal low-frequency surface circulation and topography-related currents and (2) maintained by baroclinic instabilities associated with the seasonal mixed layer and $O(10)$ km-scale submesoscale eddies with weak seasonal variability.

The KE spectra of the statistically decomposed surface currents show a similar tendency of their decay slopes of approximately k^{-2} and k^{-3} depending on the relevant variability (Figure 6d). Although the wind-driven surface currents contain diurnal and high-frequency wind responses, they primarily include subinertial responses associated with large-scale wind variability that exhibit an approximately k^{-3} decay slope (Figures 6a and 6d). Similarly, the low-frequency surface currents with a k^{-3} decay slope can be interpreted. Conversely, the tidal currents are divided into baroclinic and barotropic components; thus, in this region, the diurnal barotropic and semidiurnal baroclinic tidal surface currents are dominant (Kim et al., 2010a), and they appear as the KE spectra with decay slopes between k^{-2} and k^{-3} (Figure 6d). The residual surface currents may contain eddies, fronts, and high-frequency noise, and these currents exhibit the spectral slopes of k^{-2} in their KE spectra (Figure 6d).
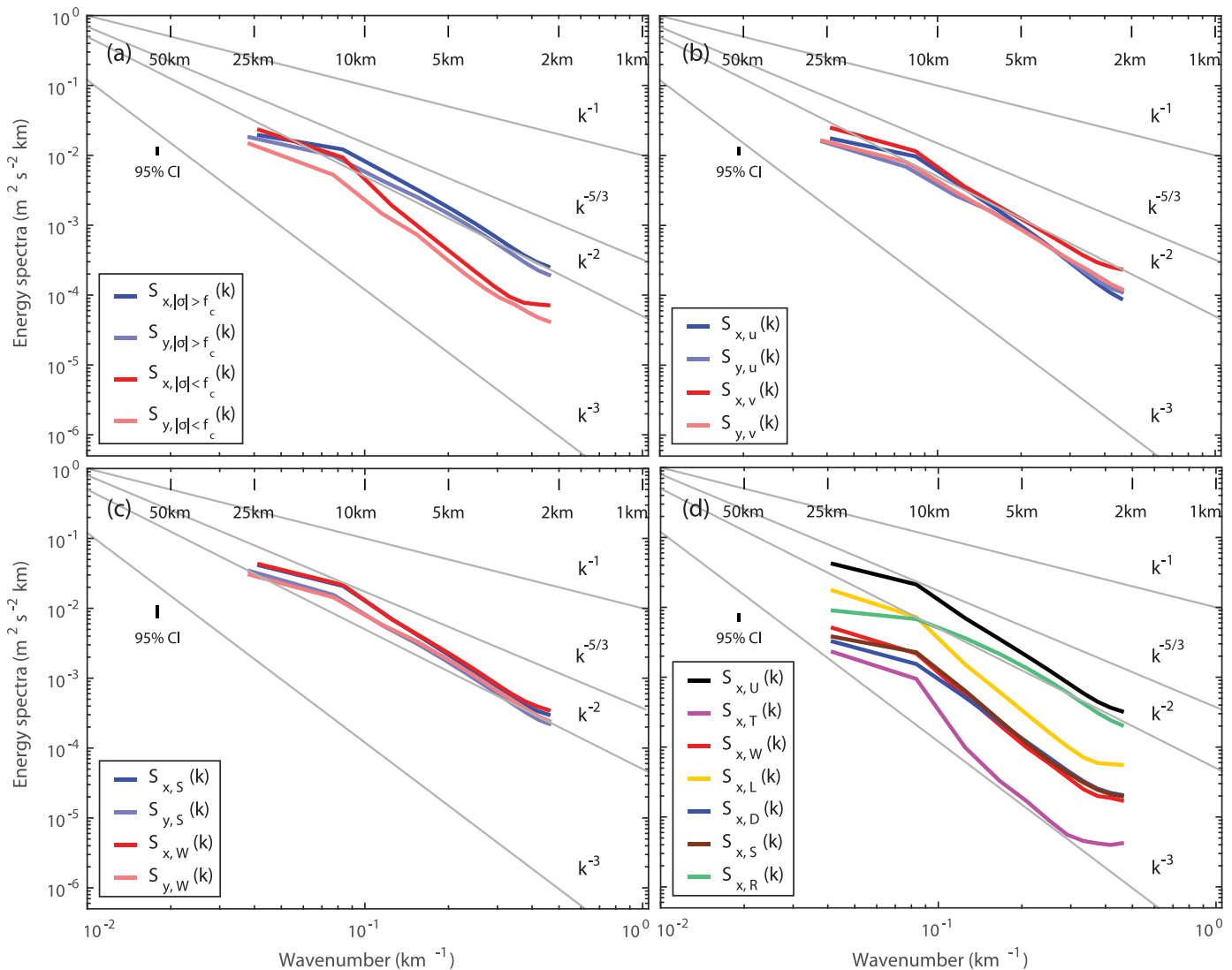
Figure 6. (a) Wave number-domain KE spectra of superinertial ($S_{,|\sigma|\geq f_c}(k)$, where f_c is the inertial frequency; blue) and subinertial ($S_{,|\sigma|<f_c}$; red) surface currents. (b) Wave number-domain KE spectra of the u-component ($S_{,u}(k)$; blue) and v-component ($S_{,v}(k)$; red) of surface currents. (c) Wave number-domain KE spectra of seasonal surface currents ($S_{,S}(k)$ for the summer; blue, $S_{,W}(k)$ for the winter; red). Darker and paler colors in Figures 6a to 6c denote the KE spectra averaged in the alongshore (x) and cross-shore (y) directions, respectively. (d) Wave number-domain KE spectra of statistically decomposed surface currents ($S_{x,\cdot}(k)$), which are averaged in the alongshore direction. Individual components of the decomposed surface currents are indicated: total surface currents ($\mathbf{u}$), surface currents coherent with pure tides ($\mathbf{u}_T$) and local wind stress ($\mathbf{u}_W$), surface currents in the low ($\mathbf{u}_L$), diurnal ($\mathbf{u}_D$), and semidiurnal ($\mathbf{u}_S$) frequency bands, and residual surface currents ($\mathbf{u}_R$). All estimates are based on the hourly surface currents for a period of 2 years (April 2003 to March 2005; 17,544 realizations). Length scales of 1, 2, 5, 10, 25, and 50 km are marked on the top, and gray auxiliary lines denote the spectral slopes of k^{-1}, $k^{-5/3}$, k^{-2}, and k^{-3}. A 95% confidence interval (CI) of individual KE spectra is indicated.

4. KE Fluxes

4.1. Estimates of KE Fluxes

A scale-by-scale energy budget equation includes the averaged cumulative measures of KE (E), KE flux (Π^*), dissipation (D), and energy injection (F) from 0 to k in the one-dimensional wave number domain (e.g., Frisch, 1995; Rhines, 1977; Scott & Wang, 2005):

$$\frac{\partial}{\partial t}E(k)+\Pi^*(k)=-D(k)+F(k). \tag{6}$$

The individual terms are formulated as follows:

$$E(k) = \frac{1}{2} \sum_{|\mathbf{k}| < k} |\hat{\mathbf{u}}(\mathbf{k})|^2, \tag{7}$$

$$\Pi^*(k) = \langle \mathbf{u}_< \cdot (\mathbf{u} \cdot \nabla \mathbf{u}) \rangle, \tag{8}$$

$$= \langle \mathbf{u}_< \cdot (\mathbf{u}_< \cdot \nabla \mathbf{u}_>) \rangle + \langle \mathbf{u}_< \cdot (\mathbf{u}_> \cdot \nabla \mathbf{u}_>) \rangle, \tag{9}$$

where $\hat{\mathbf{u}}$, $\mathbf{u}_<$, $\mathbf{u}_>$, $\langle \cdot \rangle$, and $D(k)$ denote the Fourier coefficients of currents ($\mathbf{u}$) in the wave number domain ($\mathbf{k} = (k_x, k_y)$, $k = \sqrt{k_x^2 + k_y^2}$), low-pass and high-pass filtered currents in the wave number domain, an ensemble average over a specific time window, and dissipation terms associated with coastal boundaries (e.g., bottom bathymetry and the shoreline; e.g., Scott & Wang, 2005), respectively. In this paper, the time window for ensemble averaging is chosen as six hours because this time window will maintain the regional diurnal and semidiurnal variability of the surface currents (the Nyquist frequency is equal to 2 cpd) and the improved SNRs in the KE flux estimates (see section 3.1).

The low-pass and high-pass filtered currents in the wave number domain are given by:

$$\mathbf{u}(\mathbf{x}) = \mathbf{u}_<(\mathbf{x}) + \mathbf{u}_>(\mathbf{x}), \tag{10}$$

$$= \sum_{|\mathbf{k}| < k} \hat{\mathbf{u}}(\mathbf{k}) e^{j\mathbf{k}\mathbf{x}} + \sum_{|\mathbf{k}| \geq k} \hat{\mathbf{u}}(\mathbf{k}) e^{j\mathbf{k}\mathbf{x}}. \tag{11}$$

Regarding the four terms in equation (8), two vanishing terms are described with the incompressibility of the turbulent flow fields (e.g., Frisch, 1995) as follows:

$$\langle \mathbf{u}_< \cdot (\mathbf{u}_< \cdot \nabla \mathbf{u}_<) \rangle = \langle \mathbf{u}_< \cdot (\mathbf{u}_> \cdot \nabla \mathbf{u}_<) \rangle = 0, \tag{12}$$

because the interactions between small-scale currents cannot change the variance at those scales, and the advection of small-scale currents by large-scale currents does not change the energy content of the small-scale currents.

4.2. Categorization of the Estimated KE Fluxes

As the KE fluxes are computed from the vector currents sampled from a finite spatial domain, the estimated KE flux ($\Pi^*(k)$; colored curves in Figure 7a) is a continuous subset of the true KE flux ($\Pi_t^*(k)$, a gray curve in Figure 7a) that appears within only a range of wave numbers that a given spatial sampling can resolve (colored horizontal bars in Figure 7a). Ideally, the true KE flux is converged to zero at the largest wave number (e.g., Rhines, 1977; Salmon, 1998; Scott & Wang, 2005; Vallis, 2006), but the estimated KE flux may converge to nonzero values. Thus, a relative KE flux ($\Pi(k)$) is defined as the KE flux with respect to the KE flux value at the largest wave number (k_{max}):

$$\Pi(k) = \Pi^*(k) - \Pi^*(k_{max}), \tag{13}$$

and these are referred to as the KE flux in the remainder of the paper. The uncertainty of the estimated KE fluxes is equal to 6×10^{-9} m^2 s^{-3}, which is based on the uncertainty of the observed surface currents (≈ 6 cm s^{-1}, see section 2.1). The estimated KE fluxes below the uncertainty will be noted because only relative KE fluxes are presented in the following sections.

The estimated KE fluxes are categorized into four cases of (1) all positive values ($\Pi(k) > 0$ for all k; red), (2) all negative values ($\Pi(k) < 0$ for all k; blue), (3) a single zero-crossing with a negative KE flux value at the smallest wave number ($\Pi(k) = 0$ for a single k and $\Pi(k_{min}) < 0$; black; Figures 7a and 7b), and (4) residuals and noise, which are based on the sign of the relative KE fluxes. Positive KE fluxes at all wave numbers indicate that the forward cascade of enstrophy is initiated at the scale larger than the maximum size of the domain in the spatial sampling (e.g., 25 km in this paper), which is called the baroclinic mode (e.g., Salmon, 1998; Scott & Wang, 2005). In contrast, negative KE fluxes at all wave numbers imply that the inverse cascade of energy occurs within the scales (e.g., 2 to 25 km in this paper) that can be resolved by the given observations, which is called the barotropic mode (e.g., Salmon, 1998; Scott & Wang, 2005). Thus, the forward cascades occur below the smallest spatial sampling scale (below 2 km in this paper). In addition, a single zero-crossing case indicates that the forward enstrophy cascade and inverse energy cascade occur within the scales that finite sampling can afford. On a cautionary note, the estimated zero-crossing wave number (k_o) can be higher than
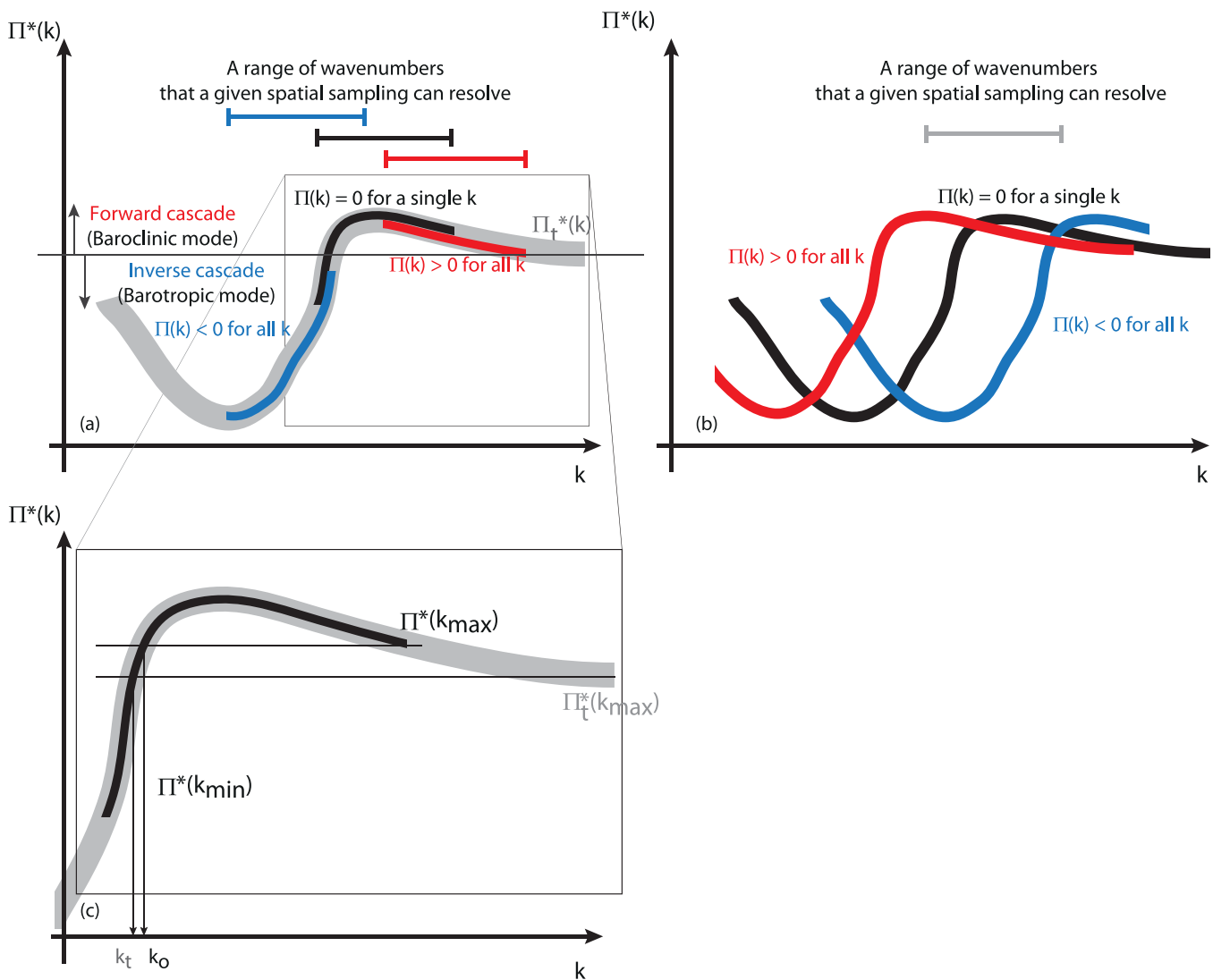
Figure 7. (a, b) True KE fluxes ($\Pi_t^*(k)$; gray) and estimated KE fluxes ($\Pi^*(k)$) for three cases of all positive values ($\Pi(k) > 0$ for all k; red) for purely forward cascades, all negative values ($\Pi(k) < 0$ for all k; blue) for purely inverse cascades, and a single zero-crossing with a negative KE flux value at the smallest wave number ($\Pi(k)=0$ for a single k and $\Pi(k_{min}) < 0$; black) for inverse-then-forward cascades are described with respect to (a) the sign of estimated KE fluxes and (b) the range of wave numbers that given spatial sampling can resolve. (c) Estimated zero-crossing wave number (k_o) and true zero-crossing wave number (k_t) ($k_t \leq k_o$) (e.g., Rhines, 1977; Salmon, 1998; Scott & Wang, 2005).

the true zero-crossing wave number (k_t) due to the finite spatial sampling of the data (Figure 7c). Thus, the estimated separation length scale in this paper can be a lower bound of the true separation length scale. Finally, the residuals may contain the cases with multiple zero-crossings, oppositely decaying patterns of the forward and inverse cascades (e.g., positive values at low wave numbers and negative values at high wave numbers), and noisy estimates. The percentages of the number of realizations for the four categorized cases (S1, S2, S3, and S4) relative to the total number of realizations are summarized in Table 1.

4.3. Interpretation of Estimated KE Fluxes
An example of the KE flux ($\Pi(k)$) estimated from a single realization of the surface currents within the white box in Figure 2a shows that the zero-crossing wave number appears between 0.06 and 0.1 km^{-1}, which corresponds to the separation length scales between 10 and 15 km (Figure 2e).

The KE fluxes are estimated from six-hourly averaged total surface currents for a period of two years (April 2003 to March 2005; 2,924 realizations) and categorized into four cases of all positive values ($\Pi(k) > 0$ for

Table 1

Fractional Distribution (%) of the Categorized KE Fluxes Into All Positive Values ($\Pi(k) > 0$ for All k; S1) for Purely Forward Cascades, All Negative Values ($\Pi(k) < 0$ for All k; S2) for Purely Inverse Cascades, a Single Zero-Crossing Having a Negative KE Flux Value at the Smallest Wave Number ($\Pi(k)=0$ for a Single k and $\Pi(k_{min}) < 0$; S3) for Inverse-Then-Forward Cascades, and Residuals (S4)

Components	S1	S2	S3	S4
u	32.7	39.6	18.8	8.9
u$_T$	39.9	42.9	10.3	6.9
u$_W$	47.6	17.7	27.2	7.5
u$_{\hat{L}}$	41.0	35.8	12.7	10.5
u$_{\hat{D}}$	38.6	37.9	15.8	7.7
u$_{\hat{S}}$	37.9	38.1	16.1	7.9
u$_R$	29.8	37.5	20.8	11.9

Note. All estimates are based on the six-hourly averaged total and decomposed surface currents for a period of 2 years (April 2003 to March 2005; 2,924 realizations). Individual components of the decomposed surface currents are indicated: total surface currents (**u**), surface currents coherent with pure tides (**u**$_T$) and local wind stress (**u**$_W$), surface currents in the low (**u**$_{\hat{L}}$), diurnal (**u**$_{\hat{D}}$), and semidiurnal (**u**$_{\hat{S}}$) frequency bands, and residual surface currents (**u**$_R$) (See Figures 9a and 9b for more details).

all k), all negative values ($\Pi(k) < 0$ for all k), a single zero-crossing with a negative KE flux value at the smallest wave number ($\Pi(k)=0$ for a single k and $\Pi(k_{min}) < 0$), and residuals. These categories account for 32.7%, 39.6%, 18.8%, and 8.9% of the total number of realizations, respectively (Table 1), and the composite means of the estimated KE fluxes at each wave number bin ($\bar{\Pi}(k)$) are shown in Figure 8a.

A probability density function (PDF) of the zero-crossing wave numbers shows that the separation length scales are clustered between 5 and 12 km, which is the lower bounds of the true injection scale (Figure 8b). The estimated single zero-crossing wave numbers are not caused by statistical noise, which was determined from an evaluation on the difference between positive and negative KE fluxes at the wave numbers nearest to the zero-crossing wave number (see Appendix C for details on the statistical significance of the zero-crossing wave numbers).

The regional surface circulation is characterized by (1) weak seasonal low-frequency surface circulation and topography-related currents and (2) submesoscale eddies with diameters of 5 to 15 km and Rossby number magnitudes of 0.2 to 2 (Kim, 2010), which initiate and maintain the regional submesoscale processes along with the baroclinic instabilities associated with the seasonal mixed layer (section 3.3). Thus, the weak seasonal baroclinic instability that is linked to the topography is the primary source of oceanic energy injected into the submesoscale coastal currents.

Similarly, the estimated KE fluxes of the decomposed surface currents are categorized into four cases, and their fractional distributions are summarized in Table 1. Approximately 75% of the total number of realizations accounts for purely forward and inverse cascades at all wave numbers (or 39% and 35% for each case with minor differences depending on the decomposed components), and approximately 17% and 9% of the total number of realizations constitute the single zero-crossing cases within the range of wave numbers and residuals (or noise), respectively (Table 1). The wave number-bin-averaged KE fluxes ($\bar{\Pi}_{\{\cdot\}}(k)$) and PDFs of zero-crossing wave numbers are shown in Figures 9a and 9b, respectively. Under the observational range
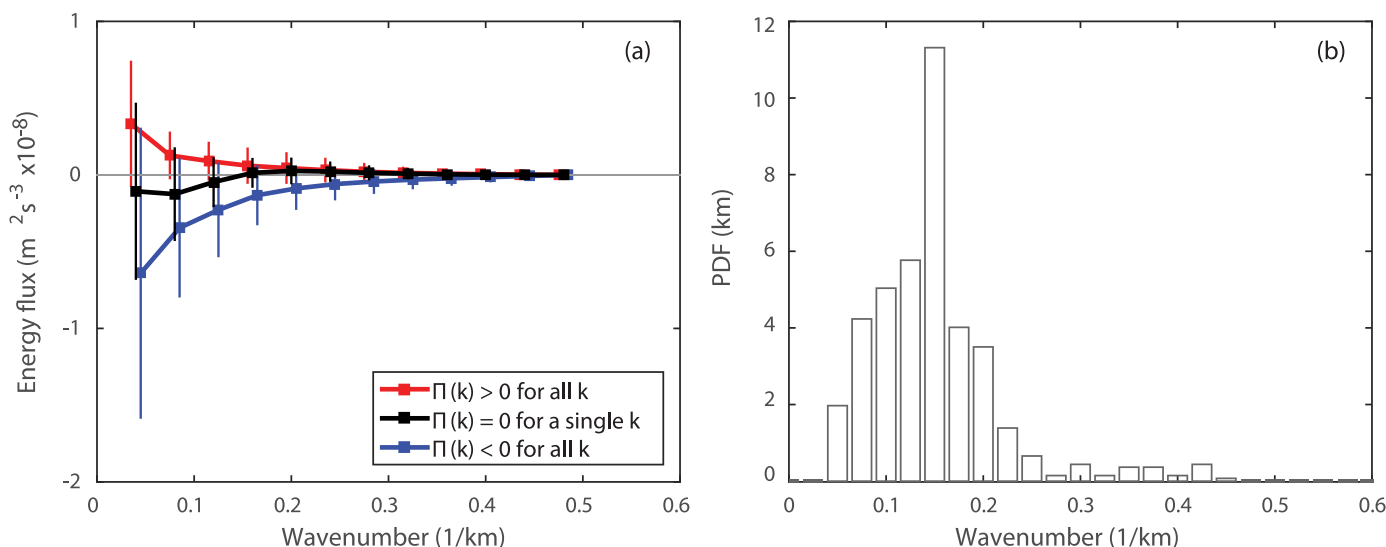

Figure 8. (a) KE fluxes ($\bar{\Pi}(k)$) compositely averaged in each wave number bin for three conditionally categorized cases of all positive values ($\Pi(k) > 0$ for all k; red) for purely forward cascades, all negative values ($\Pi(k) < 0$ for all k; blue) for purely inverse cascades, and a single zero-crossing with a negative KE flux value at the smallest wave number ($\Pi(k)=0$ for a single k and $\Pi(k_{min}) < 0$; black) for inverse-then-forward cascades. Individual KE fluxes are slightly shifted in the x axis to avoid overlapping of error bars. (b) A probability density function (PDF) of the zero-crossing wave numbers for inverse-then-forward cascades (S3). A bin size of the PDF is equal to 0.25 km^{-1}. All estimates are based on the six-hourly averaged surface currents for a period of two years (April 2003 to March 2005; 2,924 realizations).
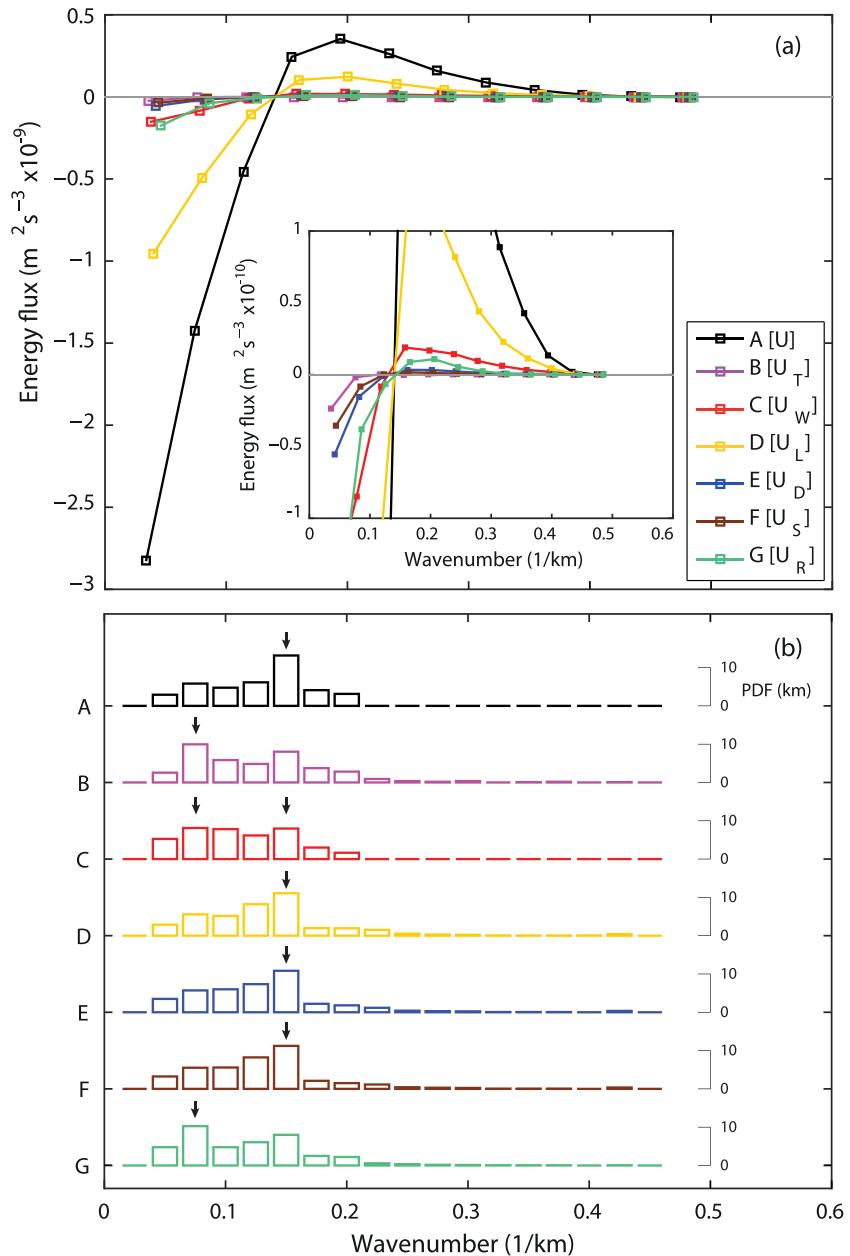
Figure 9. (a) Bin-averaged KE fluxes of the decomposed surface currents ($\bar{\Pi}_{\{\cdot\}}(k)$) at each wave number and their magnified views. (b) PDFs of the zero-crossing wave numbers of the decomposed surface currents ($k_{\{\cdot\}}$). Individual components of the decomposed surface currents are indicated: total surface currents ($\mathbf{u}$; A), surface currents coherent with pure tides ($\mathbf{u}_T$; B) and local wind stress ($\mathbf{u}_W$; C), surface currents in the low ($\mathbf{u}_L$; D), diurnal ($\mathbf{u}_D$; E), and semidiurnal ($\mathbf{u}_S$; F) frequency bands, and residual surface currents ($\mathbf{u}_R$; G). Black arrows indicate the wave number bin(s) with relatively high values of PDFs. All estimates are based on the six-hourly averaged surface currents for a period of two years (April 2003 to March 2005; 2,924 realizations).

of length scales (2 to 25 km) that the sampled surface current can resolve, the dominant injection scales appear within the range of 7 to 13 km (Figures 7 and 9b).

In these estimates, the single zero-crossing cases are highlighted on the time axis of the decomposed surface currents (Figure 3). The time windows that participate in the computation of the bin-averaged KE fluxes are different from the individual components because it is impossible to identify a time stamp that has a single zero-crossing for all decomposed surface currents at the same time. Thus, the mathematical sum of

the composite mean of the KE fluxes of the decomposed surface currents may not be equal to the KE fluxes of the total surface currents (Figure 9a):

$$\bar{\Pi}_W + \bar{\Pi}_{\hat{L}} + \bar{\Pi}_T + \bar{\Pi}_{\hat{D}} + \bar{\Pi}_{\hat{S}} + \bar{\Pi}_R \neq \bar{\Pi}. \tag{14}$$

As mentioned above, the decomposition analysis on the surface currents allows for nonlinear interactions associated with energy exchange at different wave numbers within each decomposed component instead of among individual decomposed components because (1) the decomposition analysis is based on the coherent relationships between direct driving forces and the responses and (2) there is no way to isolate the overlapping variance associated with the nonlinear interactions of two different responses. Although there might be a chance that the nonlinear interactions between the different driving forces and responses are significant, we do not interpret the detailed dynamics until the KE flux estimates obtained from the submesoscale numerical models that are driven by individual driving forces and a combination of multiple driving forces are evaluated.

5. Discussion

5.1. Spectral Decay Slopes and Injection Scales at the Submesoscale

The spectral decay slopes of the KE spectra of the submesoscale coastal surface currents are between k^{-2} and k^{-3} at the $O(1)$ km scale and commonly become steeper near the 12 km scale (Figures 5 and 6). This result can provide a glimpse of the injection scale where the inverse energy cascade and the forward enstrophy cascade occur (e.g., Vallis, 2006, Figure 8.13b), although the finite wave number may have limits to resolve the variance at a low wave number (longer than 25 km). Thus, the QG theory ($k^{-5/3}$ for inverse and k^{-3} for forward cascades) may be a theoretical framework to explain the turbulent cascades of the given observations rather than the sQG theory (k^{-1} for inverse and $k^{-5/3}$ for forward cascades; see Appendix A for more details). In addition, the separation length scale of 5 to 10 km obtained from the KE fluxes of the submesoscale coastal surface currents is consistent with where the spectral decay slopes of the KE spectra become steeper. Brink (2016) reported that the horizontal density gradient over the continental shelf becomes unstable at a spatial scale of $O(1$ to $10)$ km and leads to the generation of submesoscale eddies through a release of the mixed layer baroclinic instability into APE, which may be relevant to our observations and analysis. Thus, the regional submesoscale processes are initially energized by the weak seasonal surface frontogenesis due to regional low-frequency currents and topography-related variability, then maintained by baroclinic instability associated with the seasonal mixed layer (e.g., Callies et al., 2016; Mensa et al., 2013; Sasaki et al., 2014) because of topographically linked vortical flows and eddies with diameters of 5 to 15 km and Rossby number magnitudes of 0.2 to 2 (e.g., Kim, 2010; Kim et al., 2011), which appears as weak seasonality in the KE spectra of the surface currents (Figure 6c).

Furthermore, the KE spectra of the surface currents under rough bathymetric effects (depths deeper than 1,000 m) have been reported with a spectral decay slope of $k^{-2.5}$ (e.g., Nikurashin et al., 2013), which is in the range of our estimated spectral decay slopes and can be interpreted in the context of coastal surface currents influenced by bottom topography.

5.2. HFR-Derived Surface Currents as a Resource for Submesoscale Process Studies

The oceanic injection scales have been reported to be $O(100)$ km based on the KE fluxes computed from the ALT-derived gridded geostrophic currents (e.g., Scott & Wang, 2005), which may not resolve the currents at scales less than 100 km (e.g., Kim et al., 2011; Stammer, 1997). Thus, the KE spectra and fluxes estimated from the HFR-derived surface currents allow us to provide an extended and detailed discussion of the theoretical frameworks that can be used to explain the physical processes and KE fluxes at the $O(1-10)$ km scale.

The two-dimensional current fields are required in the estimates of the KE fluxes. Thus, the observations associated with one-dimensional along-track samplings (e.g., ALT-derived cross-track currents and shipboard ADCP-derived currents) may not be used for the KE flux studies. In addition, multiple satellite missions that are associated with observations of submesoscale processes have been developed to observe sea surface heights (SSHs) in coastal regions, including the surface water and ocean topography (SWOT) mission (e.g., Durand et al., 2010; Fu, 2010; Fu & Ferrari, 2008) and the coastal and ocean measurement mission using precise and innovative radar altimeters (COMPIRA; e.g., Uematsu et al., 2013). However, it may be difficult to retrieve ageostrophic currents from pure SSHs obtained from these high-resolution satellite missions without additional observations and model outputs. Thus, the HFR-derived surface current maps can be

used as a unique resource to investigate submesoscale processes. In particular, these vector current maps can be used for the KE flux estimates as the present-day ocean observations.

5.3. Complementary Analysis of the One-Dimensional KE Spectra

The one-dimensional wave number-domain KE spectra may have limited views for examining the characteristics of turbulent flows along the chosen sampling axis when the anisotropic current fields are considered (Appendix B). Thus, two-dimensional energy spectra via two-dimensional spatial covariances (or correlations) allow us to identify the primary directions of the variability and coastal boundary effects in terms of the anisotropy of the turbulent flows. Moreover, this approach allows us to not only use the available data most effectively (even that close to the complex coastal boundaries and nonrectangular domain) but also reduce the computational loads by repeating the computations of the one-dimensional wave number-domain KE spectra in all possible directions and interpolating or gridding the data when the data are missing. This approach is useful for quantifying decorrelation length scales using a normalized structure of spatial covariance functions, i.e., spatial correlations. For example, the locally averaged spatial correlations of the HFR-derived surface currents off of the west coast of the U.S. exhibit both Gaussian and exponential function shapes. However, their sharp decays near the zero spatial lags can be reasonably approximated with either a two-dimensional exponential function or a combination of the noise at the zero lag and an exponential or Gaussian function (e.g., Kim et al., 2010a; Roesler et al., 2013). The principal axes of the estimated correlation functions are not always aligned with the typical meridional and zonal directions, which identifies the need for a careful analysis of the one-dimensional wave number-domain KE spectra.

5.4. Spectral Decay Slopes: A Sensitive Measure of Characterizing Geophysical Turbulent Flows

The decay slopes of the oceanic KE spectra have been used to determine a theoretical framework of turbulent flow fields. However, the undersampled and sparse oceanic data provide limited information for characterizing oceanic processes (e.g., Armi & Flament, 1985; Lesieur & Sadourny, 1981). Moreover, the KE spectra of dynamic variables reflect the anisotropic and asymmetric processes caused by the coastal boundary conditions (e.g., shoreline and bathymetry). Thus, two-dimensional covariance functions can be used to examine (1) the decay slopes of KE spectra in all directions and (2) the relevant decorrelation scales using an equivalent relationship between the covariance functions in the spatial domain and the KE spectra in the wave number domain. In addition, the KE spectra of dynamic variables (e.g., currents or density) should be considered instead of those of nondynamic variables (e.g., passive tracers or chlorophyll a concentrations) when characterizing the turbulent flows because physically and dynamically irrelevant fields with the same decay slope can exist and be generated synthetically (e.g., Armi & Flament, 1985; Gower et al., 1980). However, the spectral decay slopes of the energy spectra of both dynamic and non-dynamic variables sampled in the same domain can be used as an effective tool to characterize the geophysical turbulent flows.

The use of the window function provides unambiguous estimates of the decay slope of the KE spectra. The use of the window function may reduce the original variance because the window functions transform the data sampled in a finite domain into infinitely repeated data with identical records at the beginning and end by smoothly modulating the data. Thus, the interpretation of the absolute variance of individual KE spectra can be limited.

6. Summary

Submesoscale KE spectra and fluxes at the length scales ranging from 2 to 25 km are estimated from hourly and $O(1)$ km-scale coastal surface current maps that were observed via shore-based high-frequency radars off southern San Diego. The one-dimensional wave number-domain KE spectra of the surface currents have slopes between k^{-2} and k^{-3} at a wave number (k) of 0.5 km^{-1}. The KE spectra exhibit anisotropy associated with anisotropic circulation constrained by the shoreline and the bottom bathymetry and weak seasonality related to the regional submesoscale eddies and low-frequency circulation with weak seasonal variability. Statistically decomposed surface currents are obtained from relationships between the forcings and responses in the frequency domain, which allow for the nonlinear interactions of the decomposed surface currents at all spatial scales. The one-dimensional wave number-domain KE spectra of the decomposed surface currents exhibit slopes between k^{-2} and k^{-3} depending on their variability. The

estimated KE fluxes are categorized into four cases of purely forward cascades and inverse cascades at all wave numbers, inverse-then-forward cascades with a single zero-crossing within the range of wave numbers (0.04 to 0.5 km^{-1}), and residuals, which account for approximately 33%, 39%, 19%, and 9% of the total number of realizations, respectively. An injection scale where forward enstrophy cascade and inverse energy cascade occur is estimated to be 5 to 10 km from the cases of the inverse-then-forward cascade, which is consistent with the length scales of the regional submesoscale eddies. Thus, the regional submesoscale processes are initiated by surface frontogenesis due to the weak seasonal low-frequency surface circulation and topography-related currents, and these processes are maintained by baroclinic instabilities associated with the seasonal mixed layer and $O(10)$ km-scale submesoscale eddies with weak seasonal variability.

Appendix A: Diagnostic Characteristics of Geophysical Turbulent Flows

We review the primary distinctions among the quasi-geostrophic (QG), surface QG (sQG), finite-depth sQG (fsQG), and semi-QG (SG) theories with the spectral decay slopes of one-dimensional wave number-domain KE spectra of currents at the surface and in the upper ocean as diagnostic characteristics of geophysical turbulent flow fields (e.g., Armi & Flament, 1985; Lesieur & Sadourny, 1981).

According to the QG theory, the geostrophic balance between the Coriolis force and pressure gradients under a small Rossby number is extended with inertial forces (e.g., Vallis, 2006). The KE spectra of currents under the QG theory have a decay slope of $k^{-5/3}$ for backward cascades and k^{-3} for forward cascades, which are the same for the temperature variance and conserve both total energy and potential enstrophy (e.g., Charney, 1971; Gage, 1979; Vallis, 2006).

The sQG flows are primarily driven by density evolution processes at the boundaries and are concentrated in a single vertical layer near the surface (Blumen, 1978; Held et al., 1995; Klein et al., 2009; Lapeyre & Klein, 2006; Pierrehumbert et al., 1994). Thus, the sQG theory describes the boundary dynamics more effectively than the QG theory. The conserved quantities in the sQG theory include the available (surface) potential energy (APE; or temperature variance) and the total energy. The sQG flows are decomposed into the QG solution via interior zero or constant potential vorticity (PV) and the sQG solution forced by near-surface density anomalies (e.g., Eady, 1949). According to the sQG theory, the surface current variance, which is equivalent to the temperature variance, has a decay slope of k^{-1} for inverse cascades and $k^{-5/3}$ for forward cascades (e.g., Tulloch & Smith, 2006). Specifically, the KE spectrum has a decay slope of $k^{-5/3}$ at the surface, and the decay slope of the APE grows steeper in the interior. In addition, the sQG theory is extended and is constrained by the zero PV at the bottom boundary into the fsQG theory, which maintains the QG nature at large scales, i.e., a k^{-3} decay slope, and the sQG features at small scales, i.e., a $k^{-5/3}$ decay slope (e.g., Tulloch & Smith, 2006).

In contrast, the SG theory includes the conservation of both PV and potential temperature in the QG theory and allows for their ageostrophic advection (e.g., Hoskins, 1975). The SG theory serves as an accurate framework for explaining the submesoscale dynamics related to frontogenesis and vertical circulation in relatively straight flows. The SG flows are decomposed into geostrophic and ageostrophic components (e.g., McWilliams & Gent, 1980; Thomas et al., 2009). The KE and APE in the SG theory follow a $k^{-8/3}$ power law (e.g., Andrews & Hoskins, 1978). For submesoscale flows with significant curvatures, such as curved fronts and coherent vortices, the balanced equation (BE) performs better than the SG theory (Gent et al., 1994). Although sQG and SG theories employ PV, the BE uses the stream function as a controlling scalar field (e.g., Charney, 1948; Gent et al., 1994). The KE spectrum of the horizontal velocities with a decay slope of k^{-2} can be explained by the presence of surface currents near the discontinuities in the upper ocean frontogenesis (e.g., Boyd, 1992).

Appendix B: Two-Dimensional KE Spectra and Spatial Covariances

B1. Conversion Between Two-Dimensional KE Spectra and Spatial Covariances
The KE spectra of the surface currents in space and time can be inferred from their spatial and temporal covariances, respectively. Based on the Wiener-Khinchin theorem (e.g., Cohen, 1992, 1998), the wave number-domain KE spectrum can be estimated from either the temporal mean of the squared Fourier
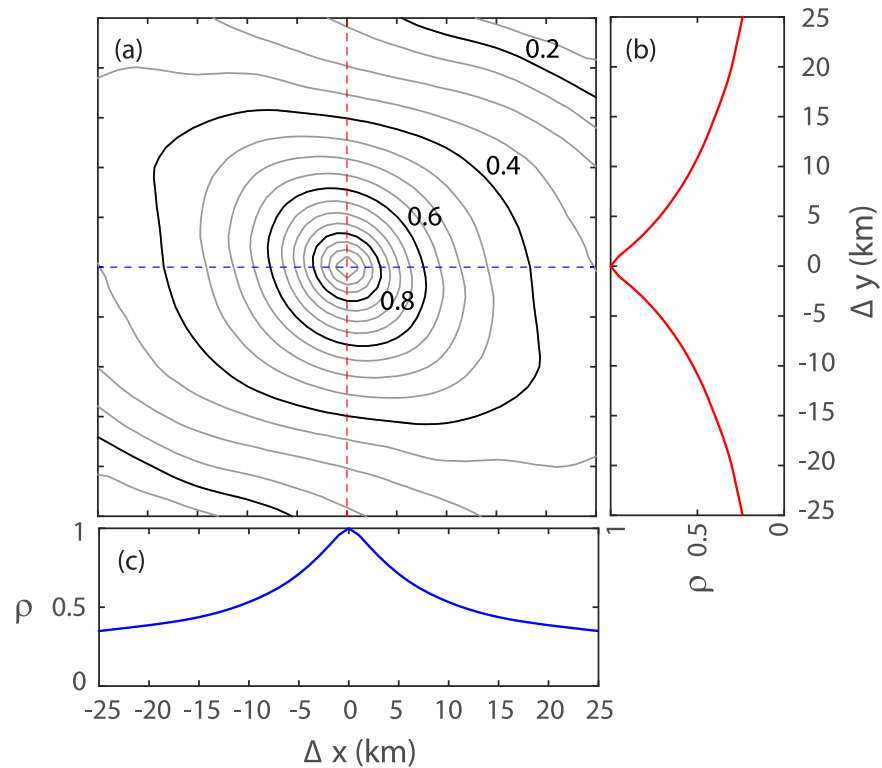
Figure B1. Examples of (a) spatial-lagged correlations ($\rho_{uu}(\Delta x, \Delta y)$) of u-components and their one-dimensional cross-sections at (b) $\Delta x = 0$ ($\rho(0, \Delta y)$) and (c) $\Delta y = 0$ ($\rho(\Delta x, 0)$). Thick black contours in Figure B1a represent correlations of 0.2, 0.4, 0.6, and 0.8 with gray contours of 0.05 spacing. Note that the spatial-lagged correlations in Figures B1a to B1c are computed from the hourly surface current within a white box in Figure 2a for a period of two years (April 2003 to March 20055; 17,544 realizations).

coefficients of the spatial data ($d(x, y, t)$ in equation (B1)) or the magnitude of the Fourier coefficients for the spatial-lagged data covariance ($c(m\Delta x, n\Delta y)$ in equation (B2)),

$$S_{\circ}(k_x, k_y) = \frac{1}{L}\sum_{l=1}^{L}\left[\frac{1}{\Delta k_x}\frac{1}{\Delta k_y}\left|\frac{1}{M}\frac{1}{N}\sum_{m=0}^{M-1}\sum_{n=0}^{N-1}d(x_m, y_n, t_l)e^{-ik_x x_m - ik_y y_n}\right|^2\right], \tag{B1}$$

$$S_{\bullet}(\alpha, \beta) = \frac{1}{\Delta \alpha}\frac{1}{\Delta \beta}\left|\frac{1}{M^*}\frac{1}{N^*}\sum_{m=-M+1}^{M-1}\sum_{n=-N+1}^{N-1}c(m\Delta x, n\Delta y)e^{-i\alpha m\Delta x - i\beta n\Delta y}\right|, \tag{B2}$$

where

$$c(m\Delta x, n\Delta y) = \frac{1}{L^*}\sum_{l=1}^{L^*}d(x, y, t_l)d(x+m\Delta x, y+n\Delta y, t_l)^{\dagger}, \tag{B3}$$

and k_x and α are wave numbers in the x direction, k_y and β are wave numbers in the y direction, and L is the number of total temporal records. M and N are the number of spatial records in the x and y directions, respectively ($M^* = 2M-1$ and $N^* = 2N-1$), and $\langle \cdot \rangle$ denotes an ensemble average of the data. The spatial-lagged data covariance in equation (B3) is a co-product of two data arrays at (x, y) and $(x+m\Delta x, y+n\Delta y)$ that have the same time record lengths (L) and no time lag, and it is divided by the number of contemporary records (L^*). The symbol † denotes either the matrix transpose for a real number (e.g., $d = u$ or v) or the complex conjugate transpose for a complex number (e.g., $d = u + iv$).

B2. Interpretation of Two-Dimensional Spatial Covariances

The spatial-lagged correlations $[\rho_{uu}(\Delta x, \Delta y)]$ of the u-components and their one-dimensional cross sections in the Δx and Δy domains are shown in Figures B1a, B1b, and B1c, respectively. The spatial-lagged correlations are calculated from the HFR-derived surface currents for a period of two years (April 2003 to March 2005; 17,544 realizations) within the white box in Figure 2a. Their cross-sectional views in both directions have a similar exponential decay patterns with different length scales (Figures B1b and B1c).

The spatial correlation coefficient (ρ) at a local grid point (x, y) that is rotated on its major axis (Δa), is fitted with the following exponential function:

$$\rho(\Delta a, \Delta b)|_{(x,y)} = \exp\left(-\sqrt{\frac{\Delta a^2}{\lambda_a^2} + \frac{\Delta b^2}{\lambda_b^2}}\right), \tag{B4}$$

where Δa and Δb denote the major and minor axes, respectively, which are rotated at an angle of the major axis relative to the spatial lag axes (Δx and Δy) at a local grid point (x, y). λ_a and λ_b denote the decorrelation length scales in the major and minor axes, respectively. The differences in the major and minor axes ($\lambda_a \neq \lambda_b$) and the tilt of the principal angle are interpreted as the anisotropy of the currents associated with anisotropic coastal boundary conditions and relevant regional circulation (e.g., alongshore dominant surface flows). A one-dimensional wave number spectrum with a decay slope of k^{-2} (or a two-dimensional wave number spectrum with a decay slope of k^{-3}) can be approximated as an exponentially decaying covariance function in a physical space (e.g., Cohen, 1992; Kim et al., 2010a; Wortham et al., 2014; Ubelmann et al., 2018):

$$\int_{-\infty}^{\infty} e^{-\frac{|x|}{a}} e^{-ikx} \mathrm{d}x = \frac{2a}{1 + a^2 k^2}, \tag{B5}$$

$$\int_{-\infty}^{\infty} \int_{-\infty}^{\infty} e^{-\sqrt{\frac{x^2}{a^2} + \frac{y^2}{b^2}}} e^{-ikx} e^{-ily} \mathrm{d}x \mathrm{d}y = \frac{2\pi ab}{(1 + a^2 k^2 + b^2 l^2)^{3/2}}, \tag{B6}$$

where a and b denote the decorrelation length scales in the x and y directions, respectively.

Similarly, the spectral decay slopes of the decomposed surface currents are deduced from their covariance functions, which allows for the examination of the dependence between the decay slopes and driving forces. Most of the two-dimensional covariance functions of the individual surface currents, including the near-inertial surface currents, have exponentially decaying shapes (Kim et al., 2010a, Figures 7 and 8). Based on the work of Kim et al. (2010a), the wind-coherent and barotropic tide-coherent surface currents have relatively broad shapes near the zero spatial lag and are close to the exponential correlation functions considering the tails and decaying structures in the spatial lags. Thus, the spectral decay slopes of the decomposed surface currents are in the range of k^{-2} and k^{-3} in the one-dimensional wave number domain but have different amplitudes and decorrelation length scales depending on the driving forces.

Appendix C: Statistical Significance of the Estimated Zero-Crossing Wave Numbers

The statistical significance of the single zero-crossing wave number (k_0) in the estimated KE fluxes is evaluated with the positive and negative values ($\Pi(k_n)$ and $\Pi(k_p)$) at the wave numbers (k_n and k_p) nearest to the candidate single zero-crossing wave number (Figure C1a).

A typical range of estimated KE fluxes is between $O(10^{-7})$ and $O(10^{-10})$ m² s⁻³. A scatter plot of the positive and negative values of the KE fluxes on both sides of the zero-crossing wave number shows that the KE fluxes near the zero-crossing wave number vary between $O(10^{-8})$ and $O(10^{-12})$ m² s⁻³ (Figure C1b). When two different threshold values are applied, the scatter plots are consistent (not shown). Thus, the estimated KE fluxes on both sides of the candidate zero-crossing wave number are significantly different from zero,
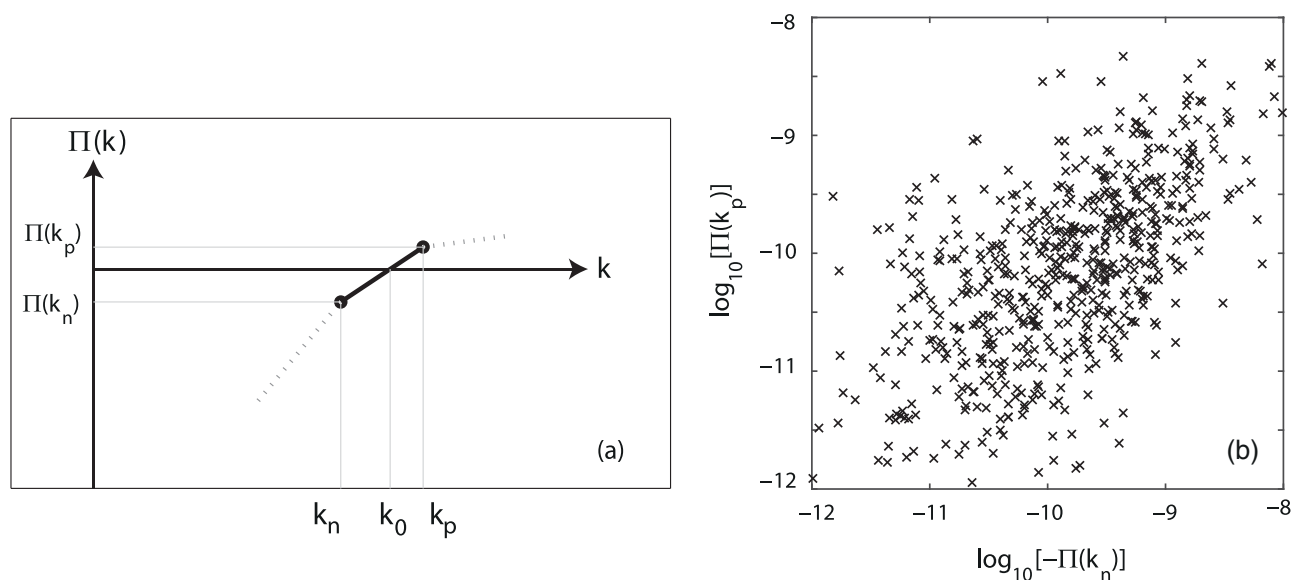
Figure C1. (a) A close-up view of the KE flux under a single zero-crossing (k_0) with a negative KE flux value at the smallest wave number ($\Pi(k)=0$ for a single k and $\Pi(k_{\min}) < 0$) in the finite wave number between negative ($\Pi(k_n)$) and positive ($\Pi(k_p)$) KE fluxes at the wave numbers (k_n and k_p) nearest to the zero-crossing wave number (k_0). (b) A scatterplot of negative ($-\Pi(k_n)$) and positive ($\Pi(k_p)$) KE fluxes at the wave numbers nearest to the single zero-crossing wave number.

implying that the estimated single zero-crossing wave numbers are not generated from either statistical noise or estimation error.

References

Andrews, D., & Hoskins, B. (1978). Energy spectra predicted by semi-geostrophic theories of frontogenesis. *Journal of the Atmospheric Sciences*, *35*, 509–512. https://doi.org/10.1175/1520-0469(1978)035<0509:ESPBSG>2.0.CO;2

Arbic, B. K., Polzin, K. L., Scott, R. B., Richman, J. G., & Shriver, J. F. (2012). On eddy viscosity, energy cascades, and the horizontal resolution of gridded satellite altimeter products. *Journal of Physical Oceanography*, *43*(2), 283–300. https://doi.org/10.1175/JPO-D-11-0240.1

Armi, L., & Flament, P. (1985). Cautionary remarks on the spectral interpretation of turbulent flows. *Journal of Geophysical Research: Oceans*, *90*(C6), 11779–11782. https://doi.org/10.1029/JC090iC06p11779

Blumen, W. (1978). Uniform potential vorticity flow: Part I. Theory of wave interactions and two-dimensional turbulence. *Journal of the Atmospheric Sciences*, *35*(5), 774–783. https://doi.org/10.1175/1520-0469(1978)035<0774:UPVFPI>2.0.CO;2

Boccaletti, G., Ferrari, R., & Fox-Kemper, B. (2007). Mixed layer instabilities and restratification. *Journal of Physical Oceanography*, *37*(9), 2228–2250. https://doi.org/10.1175/JPO3101.1

Boyd, J. P. (1992). The energy spectrum of fronts: Time evolution of shocks in Burgers' equation. *Journal of the Atmospheric Sciences*, *49*(2), 128–139. https://doi.org/10.1175/1520-0469(1992)049<0128:TESOFT>2.0.CO;2

Brink, K. H. (2016). Continental shelf baroclinic instability. Part I: Relaxation from upwelling or downwelling. *Journal of Physical Oceanography*, *46*(2), 551–568. https://doi.org/10.1175/JPO-D-15-0047.1

Buckingham, C. E., Naveira Garabato, A. C., Thompson, A. F., Brannigan, L., Lazar, A., Marshall, D. P., et al. (2016). Seasonality of submesoscale flows in the ocean surface boundary layer. *Geophysical Research Letters*, *43*, 2118–2126. https://doi.org/10.1002/2016GL068009

Buhler, O., Callies, J., & Ferrari, R. (2014). Wave–vortex decomposition of one-dimensional ship-track data. *Journal of Fluid Mechanics*, *756*, 1007–1026. https://doi.org/10.1017/jfm.2014.488

Callies, J., & Ferrari, R. (2013). Interpreting energy and tracer spectra of upper-ocean turbulence in the submesoscale range (1–200 km). *Journal of Physical Oceanography*, *43*(11), 2456–2474. https://doi.org/10.1175/JPO-D-13-063.1

Callies, J., Ferrari, R., Klymak, J. M., & Gula, J. (2015). Seasonality in submesoscale turbulence. *Nature Communications*, *6*, 6862. https://doi.org/10.1038/ncomms7862

Callies, J., Flierl, G., Ferrari, R., & Fox-Kemper, B. (2016). The role of mixed-layer instabilities in submesoscale turbulence. *Journal of Fluid Mechanics*, *788*, 5–41. https://doi.org/10.1017/jfm.2015.700

Charney, J. G. (1948). On the scale of atmospheric motions. *Geofysiske Publikasjoner*, *17*(2), 1–17.

Charney, J. G. (1971). Geostrophic turbulence. *Journal of the Atmospheric Sciences*, *28*, 1087–1095. https://doi.org/10.1175/1520-0469(1971)028<1087:GT>2.0.CO;2

Chelton, D. B., & Schlax, M. G. (1996). Global observations of oceanic Rossby waves. *Science*, *272*, 234–238. https://doi.org/10.1126/science.272.5259.234

Cohen, L. (1992). Convolution, filtering, linear systems, the Wiener-Khinchin theorem: Generalizations. *International Society for Optical Engineering*, *1770*, 378–393. https://doi.org/10.1117/12.130944

Cohen, L. (1998). Generalization of the Wiener-Khinchin theorem. *IEEE Signal Processing Letters*, *5*(11), 292–294.

D'Asaro, E., Lee, C., Rainville, L., Harcourt, R., & Thomas, L. (2011). Enhanced turbulence and energy dissipation at ocean fronts. *Science*, *332*(6027), 318–322. https://doi.org/10.1126/science.1201515

Durand, M., Fu, L.-L., Lettenmaier, D. P., Alsdorf, D. E., Rodriguez, E., & Esteban-Fernandez, D. (2010). The surface water and ocean topography mission: Observing terrestrial surface water and oceanic submesoscale eddies. *Proceedings of the IEEE*, *98*(5), 766–779. https://doi.org/10.1109/JPROC.2010.2043031

Eady, E. T. (1949). Long waves and cyclone waves. *Tellus*, *1*(3), 33–52. https://doi.org/10.1111/j.2153-3490.1949.tb01265.x

Ferrari, R., & Wunsch, C. (2009). Ocean circulation kinetic energy: Reservoirs, sources, and sinks. *Annual Review of Fluid Mechanics*, *41*, 253–282. https://doi.org/10.1146/annurev.fluid.40.111406.102139

Frisch, U. (1995). *Turbulence: The legacy of A. N. Kolmogorov* (296 pp.). Cambridge, UK: Cambridge University Press.

Fu, L.-L. (2010). Determining ocean circulation and sea level from satellite altimetry: Progress and challenges. In *Oceanography from space* (pp. 147–163). Berlin, Germany: Springer.

Fu, L.-L., & Ferrari, R. (2008). Observing oceanic submesoscale processes from space. *Eos, Transactions American Geophysical Union*, *89*(48), 488–488. https://doi.org/10.1029/2008EO480003

Gage, K. S. (1979). Evidence for a $k^{-5/3}$ law inertial range in mesoscale two-dimensional turbulence. *Journal of the Atmospheric Sciences*, *36*(10), 1950–1954. https://doi.org/10.1175/1520-0469(1979)036<1950:EFALIR>2.0.CO;2

Gent, P., McWilliams, J., & Snyder, C. (1994). Scaling analysis of curved fronts: Validity of the balance equations and semigeostrophy. *Journal of the Atmospheric Sciences*, *51*(1), 160–163. https://doi.org/10.1175/1520-0469(1994)051<0160:SAOCFV>2.0.CO;2

Gill, A., Green, J., & Simmons, A. (1974). Energy partition in the large-scale ocean circulation and the production of mid-ocean eddies. *Deep Sea Research and Oceanographic Abstracts*, *21*(7), 499–528. https://doi.org/10.1016/0011-7471(74)90010-2

Gower, J. F. R., Denman, K. L., & Holyer, R. J. (1980). Phytoplankton patchiness indicates the fluctuation spectrum of mesoscale oceanic structure. *Nature*, *288*, 157–159. https://doi.org/10.1038/288157a0

Harris, F. J. (1978). On the use of windows for harmonic analysis with the discrete Fourier transform. *Proceedings of the IEEE*, *66*(1), 51–83. https://doi.org/10.1109/PROC.1978.10837

Haza, A. C., Özgökmen, T. M., Griffa, A., Molcard, A., Poulain, P.-M., & Peggion, G. (2010). Transport properties in small-scale coastal flows: Relative dispersion from VHF radar measurements in the Gulf of La Spezia. *Ocean Dynamics*, *60*(4), 861–882. https://doi.org/10.1007/s10236-010-0301-7

Held, I., Pierrehumbert, R., Garner, S., & Swanson, K. (1995). Surface quasi-geostrophic dynamics. *Journal of Fluid Mechanics*, *282*, 1–20. https://doi.org/10.1017/S0022112095000012

Hoskins, B. J. (1975). The geostrophic momentum approximation and the semi-geostrophic equations. *Journal of the Atmospheric Sciences*, *32*(2), 233–242. https://doi.org/10.1175/1520-0469(1975)032<0233:TGMAAT>2.0.CO;2

Hoskins, B. J., & Bretherton, F. P. (1972). Atmospheric frontogenesis models: Mathematical formulation and solution. *Journal of the Atmospheric Sciences*, *29*(1), 11–37. https://doi.org/10.1175/1520-0469(1972)029<0011:AFMMFA>2.0.CO;2

Ishihara, T., & Kaneda, Y. (2001). Energy spectrum in the enstrophy transfer range of two-dimensional forced turbulence. *Physics of Fluids*, *13*(2), 544–547. https://doi.org/10.1063/1.1336149

Kim, S. Y. (2010). Observations of submesoscale eddies using high-frequency radar-derived kinematic and dynamic quantities. *Continental Shelf Research*, *30*(15), 1639–1655. https://doi.org/10.1016/j.csr.2010.06.011

Kim, S. Y. (2015). Quality assessment techniques applied to surface radial velocity maps obtained from high-frequency radars. *Journal of Atmospheric and Oceanic Technology*, *32*(10), 1915–1927. https://doi.org/10.1175/JTECH-D-14-00207.1

Kim, S. Y., & Cornuelle, B. D. (2015). Coastal ocean climatology of temperature and salinity off the Southern California Bight: Seasonal variability, climate index correlation, and linear trend. *Progress in Oceanography*, *138*, 136–157. https://doi.org/10.1016/j.pocean.2015.08.001

Kim, S. Y., Cornuelle, B. D., & Terrill, E. J. (2009). Anisotropic response of surface currents to the wind in a coastal region. *Journal of Physical Oceanography*, *39*(6), 1512–1533. https://doi.org/10.1175/2009JPO4013.1

Kim, S. Y., Cornuelle, B. D., & Terrill, E. J. (2010a). Decomposing observations of high-frequency radar derived surface currents by their forcing mechanisms: Decomposition techniques and spatial structures of decomposed surface currents. *Journal of Geophysical Research: Oceans*, *115*, C12007. https://doi.org/10.1029/2010JC006222

Kim, S. Y., Cornuelle, B. D., & Terrill, E. J. (2010b). Decomposing observations of high-frequency radar derived surface currents by their forcing mechanisms: Locally wind-driven surface currents. *Journal of Geophysical Research: Oceans*, *115*, C12046. https://doi.org/10.1029/2010JC006223

Kim, S. Y., Gopalakrishnan, G., & Ponte, A. (2015). Interpretation of coastal wind transfer functions with momentum balances derived from idealized numerical model simulations. *Ocean Dynamics*, *65*(1), 115–141. https://doi.org/10.1007/s10236-014-0766-x

Kim, S. Y., & Kosro, P. M. (2013). Observations of near-inertial surface currents off Oregon: Decorrelation time and length scales. *Journal of Geophysical Research: Oceans*, *118*, 3723–3736. https://doi.org/10.1002/jgrc.20235

Kim, S. Y., Terrill, E. J., & Cornuelle, B. D. (2007). Objectively mapping HF radar-derived surface current data using measured and idealized data covariance matrices. *Journal of Geophysical Research: Oceans*, *112*, C06021. https://doi.org/10.1029/2006JC003756

Kim, S. Y., Terrill, E. J., & Cornuelle, B. D. (2008). Mapping surface currents from HF radar radial velocity measurements using optimal interpolation. *Journal of Geophysical Research: Oceans*, *113*, C10023. https://doi.org/10.1029/2007JC004244

Kim, S. Y., Terrill, E. J., Cornuelle, B. D., Jones, B., Washburn, L., Moline, M. A., et al. (2011). Mapping the U.S. West Coast surface circulation: A multiyear analysis of high-frequency radar observations. *Journal of Geophysical Research: Oceans*, *116*, C03011. https://doi.org/10.1029/2010JC006669

Klein, P., Hua, B. L., Lapeyre, G., Capet, X., Le Gentil, S., & Sasaki, H. (2008). Upper ocean turbulence from high-resolution 3D simulations. *Journal of Physical Oceanography*, *38*(8), 1748–1763. https://doi.org/10.1175/2007JPO3773.1

Klein, P., Isern-Fontanet, J., Lapeyre, G., Roullet, G., Danioux, E., Chapron, B., et al. (2009). Diagnosis of vertical velocities in the upper ocean from high resolution sea surface height. *Geophysical Research Letters*, *36*, L12603. https://doi.org/10.1029/2009GL038359

Lapeyre, G., & Klein, P. (2006). Impact of the small-scale elongated filaments on the oceanic vertical pump. *Journal of Marine Research*, *64*(6), 835–851. https://doi.org/10.1357/002224006779698369

Larichev, V. D., & Held, I. M. (1995). Eddy amplitudes and fluxes in a homogeneous model of fully developed baroclinic instability. *Journal of Physical Oceanography*, *25*(10), 2285–2297. https://doi.org/10.1175/1520-0485(1995)025<2285:EAAFIA>2.0.CO;2

Lekien, F., & Coulliette, C. (2007). Chaotic stirring in quasi-turbulent flows. *Philosophical Transactions of the Royal Society A*, *365*, 3061–3084. https://doi.org/10.1098/rsta.2007.0020

Lesieur, M., & Sadourny, R. (1981). Satellite-sensed turbulent ocean structure. *Nature*, *294*, 673. https://doi.org/10.1038/294673a0

Le Traon, P., Klein, P., Hua, B., & Dibarboure, G. (2008). Do altimeter wavenumber spectra agree with the interior or surface quasigeostrophic theory? *Journal of Physical Oceanography*, *38*(5), 1137–1142. https://doi.org/10.1175/2007JPO3806.1

Levy, M., Ferrari, R., Franks, P. J., Martin, A. P., & Riviere, P. (2012). Bringing physics to life at the submesoscale. *Geophysical Research Letters*, *39*, L14602. https://doi.org/10.1029/2012GL052756

Lindborg, E. (2015). A Helmholtz decomposition of structure functions and spectra calculated from aircraft data. *Journal of Fluid Mechanics*, *762*, R4. https://doi.org/10.1017/jfm.2014.685

Longuet-Higgins, M., Gill, A., & Kenyon, K. (1967). Resonant interactions between planetary waves [and discussion]. *Proceedings of the Royal Society of London. Series A, Mathematical and Physical Sciences*, *299*(1456), 120–144. https://doi.org/10.1098/rspa.1967.0126

Mahadevan, A., & Tandon, A. (2006). An analysis of mechanism for submesoscale vertical motion at ocean fronts. *Ocean Modelling*, *14*, 241–256. https://doi.org/10.1016/j.ocemod.2006.05.006

McWilliams, J., & Gent, P. (1980). Intermediate models of planetary circulations in the atmosphere and ocean. *Journal of the Atmospheric Sciences*, *37*, 1657–1678. https://doi.org/10.1175/1520-0469(1980)037<1657:IMOPCI>2.0.CO;2

McWilliams, J. C. (1985). Submesoscale, coherent vortices in the ocean. *Reviews of Geophysics*, *23*(2), 162–182. https://doi.org/10.1029/RG023i002p00165

McWilliams, J. C. (2016). Submesoscale currents in the ocean. *Proceedings of the Royal Society of London. Series A, Mathematical and Physical Sciences*, *472*(2189), https://doi.org/10.1098/rspa.2016.0117

Mensa, J. A., Garraffo, Z., Griffa, A., Özgökmen, T. M., Haza, A., & Veneziani, M. (2013). Seasonality of the submesoscale dynamics in the Gulf Stream region. *Ocean Dynamics*, *63*(8), 923–941. https://doi.org/10.1007/s10236-013-0633-1

Munk, W., Armi, L., Fischer, K., & Zachariasen, F. (2000). Spirals on the sea. *Proceedings of the Royal Society of London. Series A, Mathematical and Physical Sciences*, *456*, 1217–1280. https://doi.org/10.1098/rspa.2000.0560

Nikurashin, M., Vallis, G., & Adcroft, A. (2013). Routes to energy dissipation for geostrophic flows in the Southern Ocean. *Nature Geoscience*, *6*(1), 48–51. https://doi.org/10.1038/ngeo1657

Paduan, J. D., Kim, K. C., Cook, M. S., & Chavez, F. P. (2006). Calibration and validation of direction-finding high-frequency radar ocean surface current observations. *IEEE Journal of Oceanic Engineering*, *31*(4), 862–875. https://doi.org/10.1109/JOE.2006.886195

Pedlosky, J. (1992). *Geophysical fluid dynamics* (2nd ed., 710 pp.). Berlin, Germany: Springer.

Pierrehumbert, R., Held, I., & Swanson, K. (1994). Spectra of local and nonlocal two-dimensional turbulence. *Chaos, Solitons & Fractals*, *4*(6), 1111–1116. https://doi.org/10.1016/0960-0779(94)90140-6

Priestley, M. B. (1981). *Spectral analysis and time series* (890 pp.). London, UK: Academic Press.

Rhines, P. B. (1977). The dynamics of unsteady currents. In *The sea: Ideas and observations on progress in the study of the seas* (Vol. 6, chap. 7, pp. 189–318). New York, NY: John Wiley.

Roesler, C., Emery, W., & Kim, S. Y. (2013). Evaluating the use of high-frequency radar coastal currents to correct satellite altimetry. *Journal of Geophysical Research: Oceans*, *118*, 3240–3259. https://doi.org/10.1002/jgrc.20220

Salmon, R. (1998). *Lectures on geophysical fluid dynamics*. Oxford, UK: Oxford University Press.

Sasaki, H., Klein, P., Qiu, B., & Sasai, Y. (2014). Impact of oceanic-scale interactions on the seasonal modulation of ocean dynamics by the atmosphere. *Nature Communications*, *5*, 5636. https://doi.org/10.1038/ncomms6636

Schmidt, R. O. (1986). Multiple emitter location and signal parameter estimation. *IEEE Transactions on Antennas and Propagation*, *34*(3), 276–280. https://doi.org/10.1109/TAP.1986.1143830

Scott, R. B., & Wang, F. (2005). Direct evidence of an oceanic inverse kinetic energy cascade from satellite altimetry. *Journal of Physical Oceanography*, *35*(9), 1650–1666. https://doi.org/10.1175/JPO2771.1

Shcherbina, A. Y., D'Asaro, E. A., Lee, C. M., Klymak, J. M., Molemaker, M. J., & McWilliams, J. C. (2013). Statistics of vertical vorticity, divergence, and strain in a developed submesoscale turbulence field. *Geophysical Research Letters*, *40*, 4706–4711. https://doi.org/10.1002/grl.50919

Smith, K. S., & Vallis, G. K. (2002). The scales and equilibration of midocean eddies: Forced dissipative flow. *Journal of Physical Oceanography*, *32*(6), 1699–1720. https://doi.org/10.1175/1520-0485(2002)032<1699:TSAEOM>2.0.CO;2

Stammer, D. (1997). Global characteristics of ocean variability estimated from regional TOPEX/POSEIDON altimeter measurements. *Journal of Physical Oceanography*, *27*(8), 1743–1769. https://doi.org/10.1175/1520-0485(1997)027<1743:GCOOVE>2.0.CO;2

Thomas, L. N., Tandon, A., & Mahadevan, A. (2009). Submesoscale processes and dynamics. In *Ocean modeling in an eddying regime, Geophysical monograph series* (Vol. 177, pp. 17–38). Washington, DC: American Geophysical Union.

Tulloch, R., & Smith, K. (2006). A theory for the atmospheric energy spectrum: Depth-limited temperature anomalies at the tropopause. *Proceedings of the National Academy of Sciences of the United States of America*, *103*(40), 14690–14694. https://doi.org/10.1073/pnas.0605494103

Tung, K., & Orlando, W. (2003). The k^{-3} and $k^{-5/3}$ energy spectrum of atmospheric turbulence: Quasigeostrophic two-level model simulation. *Journal of the Atmospheric Sciences*, *60*, 824–835.

Ubelmann, C., Dibarboure, G., & Dubois, P. (2018). A cross-spectral approach to measure the error budget of the SWOT altimetry mission over the ocean. *Journal of Atmospheric and Oceanic Technology*, *35*. https://doi.org/10.1175/JTECH-D-17-0061.1

Uematsu, A., Nakamura, Nakajima, R. Y., & Yajima, Y. (2013). X-band interferometric SAR sensor for the Japanese altimetry mission, COMPIRA. In *Geoscience and Remote Sensing Symposium (IGARSS)* (pp. 2943–2946). Piscataway, NJ: IEEE.

Vallis, G. K. (2006). *Atmospheric and oceanic fluid dynamics* (745 pp.). Cambridge, UK: Cambridge University Press.

Venaille, A., Vallis, G. K., & Smith, K. S. (2011). Baroclinic turbulence in the ocean: Analysis with primitive equation and quasigeostrophic simulations. *Journal of Physical Oceanography*, *41*(9), 1605–1623. https://doi.org/10.1175/JPO-D-10-05021.1

Wang, D., Flagg, C., Donohue, K., & Rossby, H. (2010). Wavenumber spectrum in the Gulf Stream from shipboard ADCP observations and comparison with altimetry measurements. *Journal of Physical Oceanography*, *40*(4), 840–844. https://doi.org/10.1175/2009JPO4330.1

Woods, J. D. (1980). Do waves limit turbulent diffusion in the ocean? *Nature*, *288*, 219–224. https://doi.org/10.1038/288219a0

Wortham, C., Callies, J., & Scharffenberg, M. G. (2014). Asymmetries between wavenumber spectra of along- and across-track velocity from tandem-mission altimetry. *Journal of Physical Oceanography*, *44*(4), 1151–1160. https://doi.org/10.1175/JPO-D-13-0153.1

Wortham, C., & Wunsch, C. (2014). A multi-dimensional spectral description of ocean variability. *Journal of Physical Oceanography*, *44*(3), 944–966. https://doi.org/10.1175/JPO-D-13-0113.1

Wunsch, C. (2015). *Modern observational physical oceanography: Understanding the global ocean*. Princeton, NJ: Princeton University Press.

Wunsch, C., & Ferrari, R. (2004). Vertical mixing, energy, and the general circulation of the oceans. *Annual Review of Fluid Mechanics*, *36*, 281–314. https://doi.org/10.1146/annurev.fluid.36.050802.122121

Xu, Y., & Fu, L.-L. (2012). The effects of altimeter instrument noise on the estimation of the wavenumber spectrum of sea surface height. *Journal of Physical Oceanography*, *42*(12), 2229–2233. https://doi.org/10.1175/JPO-D-12-0106.1

Zhou, X.-H., Wang, D.-P., & Chen, D. (2015). Global wavenumber spectrum with corrections for altimeter high frequency noise. *Journal of Physical Oceanography*, *45*(2), 495–503. https://doi.org/10.1175/JPO-D-14-0144.1